Gondwana Research 97 (2021) 176–203

Contents lists available at ScienceDirect

Gondwana Research

journal homepage: www.elsevier.com/locate/gr

GR Focus Review

# New paleogeographic and degassing parameters for long-term carbon cycle models

Chloé M. Marcilly [a,*], Trond H. Torsvik [a,b], Mathew Domeier [a], Dana L. Royer [c]

[a] Centre for Earth Evolution and Dynamics (CEED), University of Oslo, 0315 Oslo, Norway
[b] School of Geosciences, University of Witwatersrand, Johannesburg 2050, South Africa
[c] Department of Earth and Environmental Sciences, Wesleyan University, Middletown, CT 06459, USA

ARTICLE INFO

*Article history:*
Received 22 February 2021
Revised 21 May 2021
Accepted 21 May 2021
Available online 26 May 2021
Handling Editor: M. Santosh

*Keywords:*
Carbon cycle
Modelling
Paleoclimate
Phanerozoic
Paleogeography
Degassing

ABSTRACT

Long-term carbon cycle models are critical for understanding the levels and underlying controls of atmospheric $CO_2$ over geological time-scales. We have refined the implementation of two important boundary conditions in carbon cycle models, namely consumption by silicate weathering and carbon degassing. Through the construction of continental flooding maps for the past 520 million years (Myrs), we have estimated exposed land area relative to the present-day ($f_A$), and the fraction of exposed land area undergoing silicate weathering ($f_{AW\text{-}fA}$). The latter is based on the amount of exposed land within the tropics (±10°) plus the northern/southern wet belts (±40–50°) relative to today, which are the prime regions for silicate weathering. We also evaluated climate gradients and potential weatherability by examining the distribution of climate-sensitive indicators. This is particularly important during and after Pangea formation, when we reduce $f_{AW}$-$f_A$ during times when arid equatorial regions were present. We also estimated carbon degassing for the past 410 Myrs using the subduction flux from full-plate models as a proxy. We further used the subduction flux to scale and normalize the arc-related zircon age distribution (arc-activity), allowing us to estimate carbon degassing in much deeper time. The effect of these refined modelling parameters for weathering and degassing was then tested in the GEOCARBSULFvolc model, and the results are compared to other carbon cycle models and $CO_2$ proxies. The use of arc-activity as a proxy for carbon degassing brings Mesozoic model estimates closer to $CO_2$ proxy values but our models are highly sensitive to the definition of $f_{AW}$-$f_A$. Considering only variations in the land availability to weathering that occur in tropical latitudes (corrected for arid regions) and the use of our new degassing estimates leads to notably higher $CO_2$ levels in the Mesozoic, and a better fit with the $CO_2$ proxies.



**Contents**

1. Introduction . . . 177
2. Paleogeographical maps . . . 178
 2.1. Methods . . . 178
  2.1.1. Building maps of exposed land . . . 178
  2.1.2. Estimating theoretical silicate weathering strength . . . 179
 2.2. Paleogeographic reconstructions and weatherability . . . 181
  2.2.1. Early Paleozoic (Cambrian to Silurian) . . . 181
  2.2.2. Late Paleozoic (Devonian to Permian) . . . 182
  2.2.3. Mesozoic-Cenozoic . . . 185
  2.2.4. Comparison of reconstructed weatherability with other studies . . . 185
3. Estimating degassing for long-term carbon models . . . 186
 3.1. Degassing since 250 Ma: Rates of crustal production and destruction vs. subduction lengths . . . 186
 3.2. Degassing since the Early Devonian (410 Ma) based on subduction fluxes . . . 187

* Corresponding author.
*E-mail address:* c.f.m.marcilly@geo.uio.no (C.M. Marcilly).

https://doi.org/10.1016/j.gr.2021.05.016
1751-7311/

3.3. Constraining degassing in deep time: The use of detrital zircon ages . . . 187
4. Revision of paleogeographic and degassing input parameters in GEOCARBSULFvolc . . . 189
4.1. Revision of $f_A$ and $f_{AW}$ $f_A$ . . . 191
4.2. Revised degassing ($f_{SR}$) . . . 192
5. $CO_2$ modelling . . . 193
5.1. Phanerozoic $CO_2$ fluctuations from GEOCARBSULFvolc model simulations (Royer et al., 2014) . . . 193
5.2. Revised models . . . 194
6. Discussion . . . 197
7. Conclusions and challenges . . . 199
Declaration of Competing Interest . . . 200
Acknowledgments . . . 200
Appendix A. Supplementary material . . . 200
References . . . 200

## 1. Introduction

Atmospheric $CO_2$ concentrations have fluctuated considerably over geological time, driven by time-dependent solar, tectonic, and biological forcings. A history of those fluctuations can be reconstructed from proxies of past $CO_2$ concentrations that extend back into the Paleozoic, but these proxy records are fragmentary and often associated with large uncertainties (Foster et al., 2017). In contrast, models for the long term carbon cycle, e.g. GEOCARBSULF (volc) (e.g., Berner, 2004; 2006; Royer et al., 2014), COPSE (e.g. Bergman et al., 2004; Lenton et al., 2018), and GEOCLIM (e.g., Goddéris et al., 2012, 2014; Donnadieu et al. 2006), aim to capture the principal forcings on $CO_2$ (the time-dependent balance of sources and sinks) to formulate retrodictions of its past atmospheric concentration. Modelling, therefore, plays a key role in not only reconstructing past $CO_2$ fluctuations (as a complement to the proxy record) but also our attempt to understand their causes.

The relative importance of different carbon *sinks* and *sources* is debated, and variations in forcing factors are mostly estimated by indirect methods. $CO_2$ *sinks* include silicate weathering and burial of carbonates and organic carbon (e.g., Berner et al., 1983; Berner, 2004; Walker et al., 1981; Worsley and Kidder, 1991; Otto-Bliesner, 1995; Goddéris et al., 2012, 2014). The strength of the silicate weathering feedback is largely tied to relief and climate, which in turn is linked to plate tectonics and continental paleogeography (Worsley and Kidder, 1991; Gibbs et al., 1999; Berner, 2004; Donnadieu et al., 2006; Goddéris et al., 2014; Goddéris and Donnadieu, 2017). For example, continents located at tropical latitudes, and their associated warm and wet climates, promote $CO_2$ consumption by silicate weathering. Constraining the paleogeographic input in long-term carbon cycle models is therefore fundamental (Donnadieu et al., 2006; Pohl et al., 2014; Goddéris et al., 2014; Goddéris and Donnadieu, 2017). Remarkably, Charles Lyell proposed such a link between paleogeography and the climate in 1830 (Lyell, 1830), long before Alfred Wegener presented his revolutionary theory of continental drift in 1912.

Plate tectonics plays an important role in shaping the long-term climate at both regional and global scales by controlling the distribution of continents and oceans (paleogeography), and erecting and dismantling mountain ranges, thereby modulating the intensity of weathering, but also by powering arc-volcanism, the main *source* of $CO_2$ (e.g., Gyllenhaal et al., 1991; Zhang et al., 2012; Lagabrielle et al., 2009; Hay et al., 1990; Horton et al., 2010; Barron et al., 1989; Otto-Bliesner, 1995). Volcanic emissions and metamorphic decarbonation in continental arcs, island arcs, mid-ocean ridges, and continental rifts can loosely be referred to as solid Earth or plate tectonic degassing (Berner, 2004). There is no clear consensus on how to estimate (or even how to parameterize) such degassing through geological time, but in the GEOCARBSULF model (Berner, 2004) there is a time-dependent parameter for *'seafloor production'* ($f_{SR}$) that can be considered as a proxy of plate tectonic activity and thus solid Earth $CO_2$ degassing relative to present-day. Ironically, $CO_2$ degassing from spreading ridges is probably trivial with respect to degassing from magmatic arcs and continental arcs in particular. However, on a planet that is not expanding or shrinking, seafloor production must compensate the global subduction flux (to first order; i.e. neglecting intraplate deformation), and thus $f_{SR}$ should present a useful approximate measure of global arc activity and thus solid Earth $CO_2$ degassing.

Seafloor production can be estimated directly from present-day seafloor age grids derived from marine geophysical data (magnetic anomalies), but this only provides $f_{SR}$ estimates back to the Cretaceous. For earlier times, $f_{SR}$ may be indirectly inferred from stratigraphically derived global sea-level fluctuations because variations in seafloor spreading (mid-ocean ridge volume) are the most important driver of global sea-level change (Conrad, 2013; Karlsen et al., 2020). However, this inversion is complicated by the many other time-dependent contributions to sea-level and by the difficulty of separating global (eustatic) signals from local ones. Another approach is to estimate seafloor production in deep time from full-plate models. The locations of subduction zones are generally better defined than the location of ridges in these models, so it is more sensible to estimate and discuss the subduction flux directly. Note that full-plate models, although powerful in being constrained by multiple independent sources of data, are nevertheless simplifications with significant uncertainties that grow backward in time. With respect to the subduction flux in particular, the occurrence of intra-oceanic subduction zones may be underrepresented (van der Meer et al., 2012). Recently, McKenzie et al. (2016) and Domeier et al. (2018) suggested that apparent variations in zircon production through time could mimic real fluctuations in the global subduction flux, and so analyses of zircon age spectra may provide an independent pathway toward estimating solid Earth $CO_2$ degassing through time.

Some authors have argued that the rate of seafloor production (and thus the subduction flux) has not varied significantly for the past 180 Ma (e.g. Rowley, 2002; Cogné and Humler, 2006), but that view has been repeatedly refuted by examination of extant marine magnetic anomalies (e.g., Larson, 1991; Conrad and Lithgow-Bertelloni, 2007; Seton et al., 2009; Coltice et al., 2013) and both continental (e.g., Engebretson, 1992) and full-plate tectonic models (Domeier et al. 2018; Torsvik et al. 2020). A particular triumph of the view that the seafloor production rate varies has been the recognition of a conspicuous peak in seafloor production in the Early Cretaceous (Seton et al., 2009). In this context, it is important to point out that several recent papers have attempted to estimate the past subduction flux by simply normalizing global subduction lengths (e.g. van der Meer et al., 2014; Mills et al., 2014, 2019; Wong et al. 2019), but this implicitly assumes a constant globally averaged rate of convergence. Continental rift lengths (Brune et al., 2017), or combinations of subduction and continental rift

lengths, have also been used as measures for plate tectonic degassing (Mills et al. 2019; Wong et al., 2019), but are overly simplified for the same reason—they assume the globally averaged rates of spreading and convergence (i.e. cm/yr per unit arc/ridge length) to have remained static through time.

In this study, we explore alternative ways to constrain $CO_2$ sources and sinks through geological time, with a particular focus on estimating plate tectonic degassing and the silicate weathering potential. We explore the latter by mapping out the areas of exposed land for the past 520 Myrs (Section 2) and determining how much of it was within latitude bands of high theoretical 'weatherability'. We use the term 'weatherability' to refer to the potential in silicate weathering intensity, which is controlled by the availability of land in equatorial regions and the northern and southern wet belts. For estimating plate tectonic degassing, we use the subduction flux as a proxy back to the Early Devonian (410 Ma), estimated from full-plate tectonic models (Section 3). In an attempt to proceed even further backward in time, we re-analyzed the age distribution of arc-related zircons to explore the possibility that they grossly mimic the subduction flux. Observing a good temporal correspondence between the zircon age distribution and the subduction flux since the Early Devonian, we re-scale the former to the latter to estimate absolute values of plate tectonic degassing in deeper geologic time, when plate models become increasingly uncertain. Finally, we demonstrate how the GEOCARBSULFvolc carbon cycle model responds to our updated estimates of the time-dependent exposed land area, the fraction of that area undergoing chemical weathering, and the rate of plate tectonic degassing (Sections 4 and 5).

## 2. Paleogeographical maps

### 2.1. Methods

#### 2.1.1. Building maps of exposed land

To better constrain the amount of exposed and flooded land areas through time we have created a set of new maps based on the geological record, namely sedimentological data and fossil distributions. The maps were constructed in 10 Myr intervals from the Cambrian (520 Ma) to the Late Cretaceous (70 Ma). The exposed land maps were built following the same workflow as the maps of the PALEOMAP project (Scotese 2014a, b, 2016). As such, the main framework is a combination of geological lithofacies (Scotese, 2014a, b, 2016) and paleoclimatic reconstructions (Moore and Scotese, 2010, Scotese and Moore, 2014, Boucot et al., 2013) adapted to our plate tectonic framework (Torsvik and Cocks, 2017). However, our maps differ from those of Scotese and co-workers in several important ways, because we use a different plate tectonic framework and we integrate additional data. The PALEOMAP project is based on the plate tectonic model of Scotese (2016) (http://www.earthbyte.org/paleomap-paleoatlas-for-gplates/), whereas our reconstructions are based on Torsvik and Cocks (2017) with minor refinements in the Paleo- and Neotethys domain during the late Paleozoic and early Mesozoic. Consequently, there are large discrepancies between our continental reconstructions and those of Scotese and co-workers, both in terms of absolute longitude and latitude. These differences have a major impact on the area of land estimated to lie within latitudes of high theoretical weatherability, i.e. in the tropics and the northern/southern wet belts (~±10° and ±40–50°) (Gibbs et al., 1999; Torsvik and Cocks, 2017), and so are expected to yield distinctive silicate weathering histories in carbon cycle models like GEOCARBSULF-volc or COPSE (Berner, 2004, 2006; Royer et al., 2014; Lenton et al., 2018; Mills et al., 2014, 2019).

For the construction of exposed land maps, we prioritized the paleoenvironmental reconstructions of Torsvik and Cocks (2017) as the main source (when available); for areas and periods lacking coverage, we used reconstructions from the PALEOMAP project and other sources (Fig. 1; see supplementary data 1 for details). Additional mapping was done, notably for North Africa and Europe, using detailed maps from the peri-Tethys (Dercourt et al., 2000), Tethys project (Dercourt et al., 1993), the geological atlas of Western and Central Europe (Ziegler, 1990) and the Middle East Basins evolution program (Barrier and Vrielynck, 2008).

With the base maps of exposed land area, we modified the time-dependent coastlines of the land blocks, here called polygons, according to the distribution of climatically sensitive facies. For this, we employed a database of coal, bauxites, evaporites, and tillites based on Boucot et al. (2013) but with added data and refined time-calibration (Torsvik and Cocks, 2017). We used (for example) evaporites as indicators for the location of coastal shallow basins. This method helped to constrain coastlines when we did not have matching data between the paleogeographic reconstructions of Torsvik and Cocks (2017), the PALEOMAP project and other sources. However, evaporites could also represent lake deposits and we therefore considered only large concentrations of deposits, together with gradients reflecting a transition from coast to land (using also bauxite and coal deposits, for example).

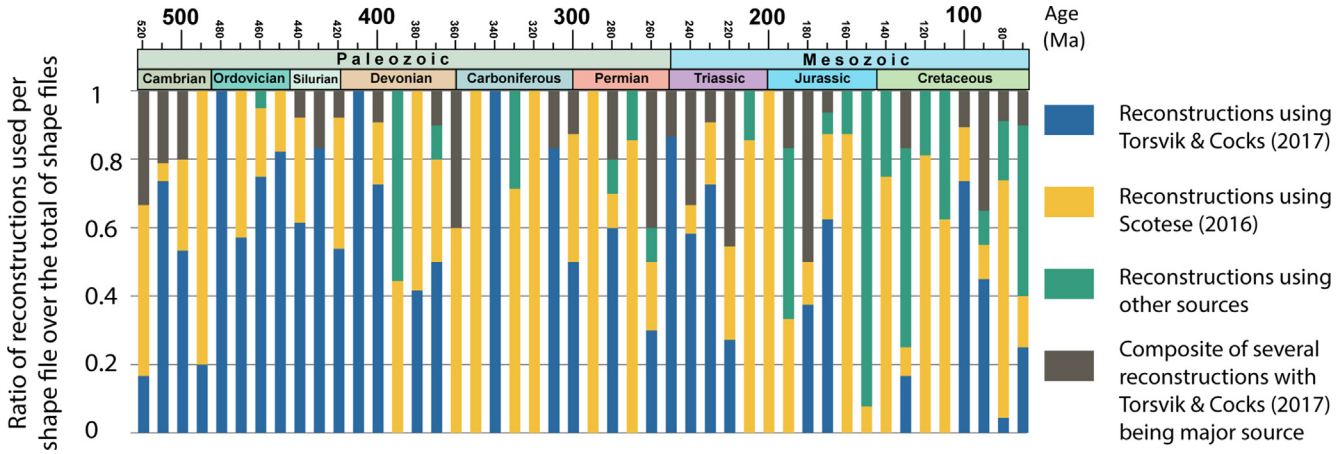


**Fig. 1.** Phanerozoic timescale and background information for the reconstructions used to build the exposed land maps (Fig. 2). The reconstructions of Torsvik and Cocks (2017) with minor refinements are always used to define the location of the continents, and the definition of land follows those maps when that information is available. The second most used source is Scotese (2016) exported in Gplates. "Composite of several reconstructions" represents the use of multiple sources in defining the land area (a complete list of sources per plate can be found in the supplementary data 1).

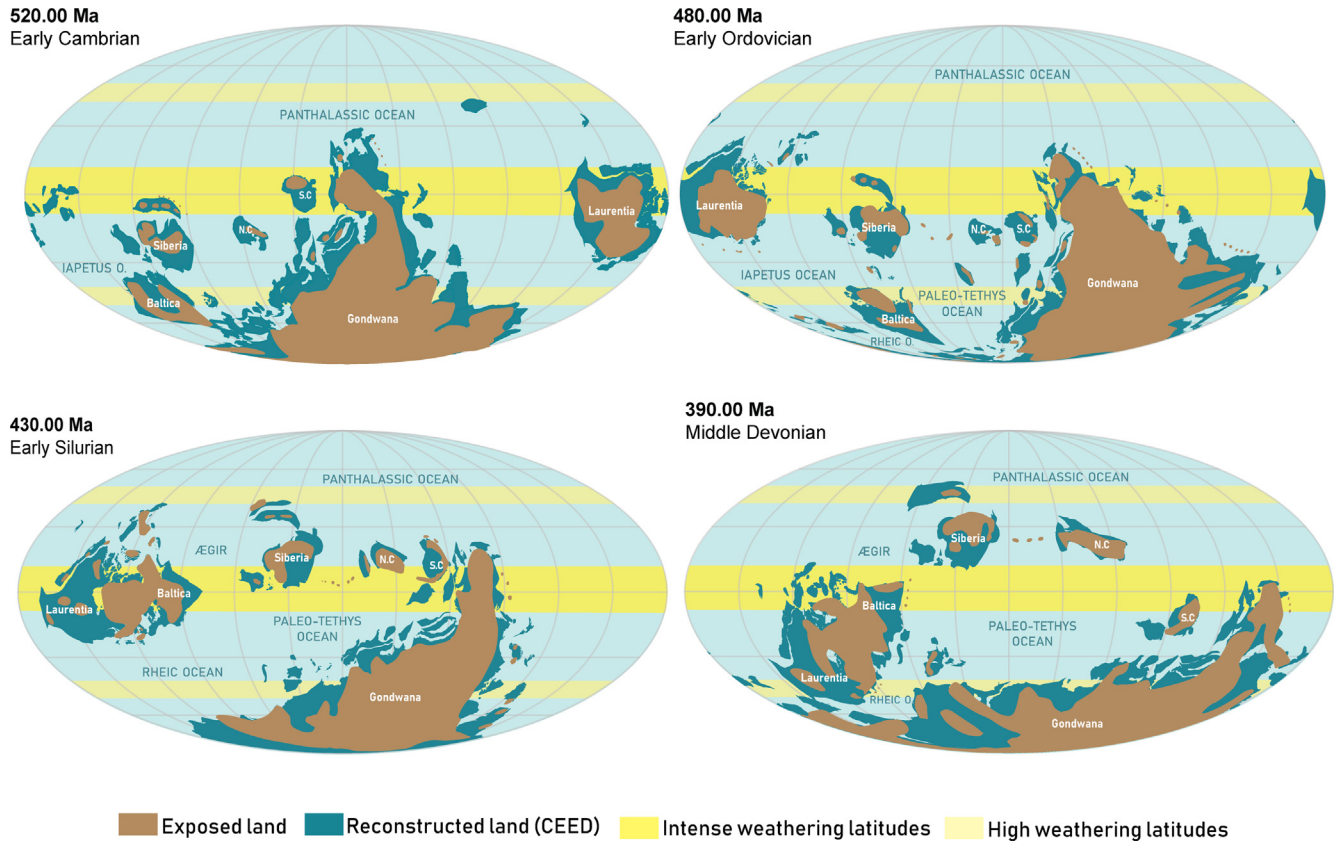


**Fig. 2.** Maps of reconstructed exposed land for the Phanerozoic (520–70 Ma). The maps are here presented for every ~50 Myrs but are originally made in 10 Myrs intervals (can be downloaded from http://www.earthdynamics.org/climate/exposed_land.zip). The blue shapes represent the contours of continents and microcontinents (CEED model: Torsvik and Cocks 2017 with updates). The brown shapes represent the exposed land, i.e. above sea-level. Three yellow bands denote the high weatherability latitudes. The more intense yellow band at ± 10° of the equator represents the latitudes of most intense chemical weathering (i.e. silicate weathering for CO2 models).

We constructed maps every 10 Myrs, although some of the underlying datasets have a coarser resolution. In some instances, a given 10 Myr interval was based in part on the extrapolation of patterns from before or after the interval (e.g., Early Carboniferous: Tournaisian; Late Triassic-Early Jurassic: Rhaetian to Sinemurian; Early Jurassic: Oxfordian). In terms of spatial uncertainty, our maps are generally continental in scale but also contain microcontinents and island arcs when available. However, they do not include all local variations that potentially could have an impact on the climate system (e.g., islands or microcontinents in the latitudes located within 10° of the equator).

Our maps of exposed land (Fig. 2) were constructed in GPlates and then used to compute the total area of exposed land at a given time, as well as the fraction of that area positioned within certain latitude bands. We also computed the same parameters from the reconstructions of Scotese (2016) and Blakey (2009). We assume that the maps of Blakey (2009), which were used for Paleozoic time in the GEOCLIM model (Goddéris et al., 2012, 2014), reflect exposed land and not total land area. Note that our maps with reconstructed land areas are constructed between 520 and 70 Ma, but we have extended our exposed land maps from 60 Ma to present-day using the maps of Golonka et al. (2006). These were digitized in Heine et al. (2015) and we used their digital outlines of exposed land transferred to the reconstructions of Torsvik and Cocks (2017). All our maps were crosschecked with the occurrences of terrestrial and marine fossils (www.paleobiodb.org) and the 60, 40 and 20 Ma maps underwent some refinements according to Poblete et al. (2021).

*2.1.2. Estimating theoretical silicate weathering strength*

Weathering plays a key role in the consumption of $CO_2$ (e.g., Walker et al. 1981), as first recognized by Ebelmen (1845), and Berner et al. (1983) and Marshall et al. (1988) were among the first to introduce weathering as a key parameter in geological carbon cycle modeling. Since then many studies have re-affirmed and further explored the linkages between weathering and carbon consumption (e.g. Francois and Walker, 1992: Goddéris and François, 1995; Goddéris and Joachimski, 2004; Goddéris et al., 2014, Mills et al., 2014), and systematic investigations of these linkages have been especially facilitated by the development of general circulation models (GCMs) (Barron et al., 1989; Otto-Bliesner, 1995).

The intensity of silicate weathering is dependent on rates of physical erosion and temperature but mostly on continental runoff, and is thus ultimately tied to plate tectonics and paleogeography through the changing of relief and the shifting of continental latitudes (White and Blum, 1995; Gibbs et al., 1999; West et al., 2005). Runoff is defined as the amount of discharge (mm/year) to the ocean relative to the amount of exposed land in a particular latitudinal band. Modern observations show that runoff is the highest, on average, in tropical latitudes between 10°N and 10°S and between 30 and 60°N (Oki and Kanae, 2006).

For large continents, and especially supercontinents such as Pangea, inland rainfall is strongly reduced and runoff is then limited by evaporation (Gibbs et al., 1999; Goddéris et al., 2014). Intervals associated with large continental assemblies, such as the late Paleozoic formation of Pangea, will thus tend to increase continentalisation of the climate, leading to aridity and the limiting of

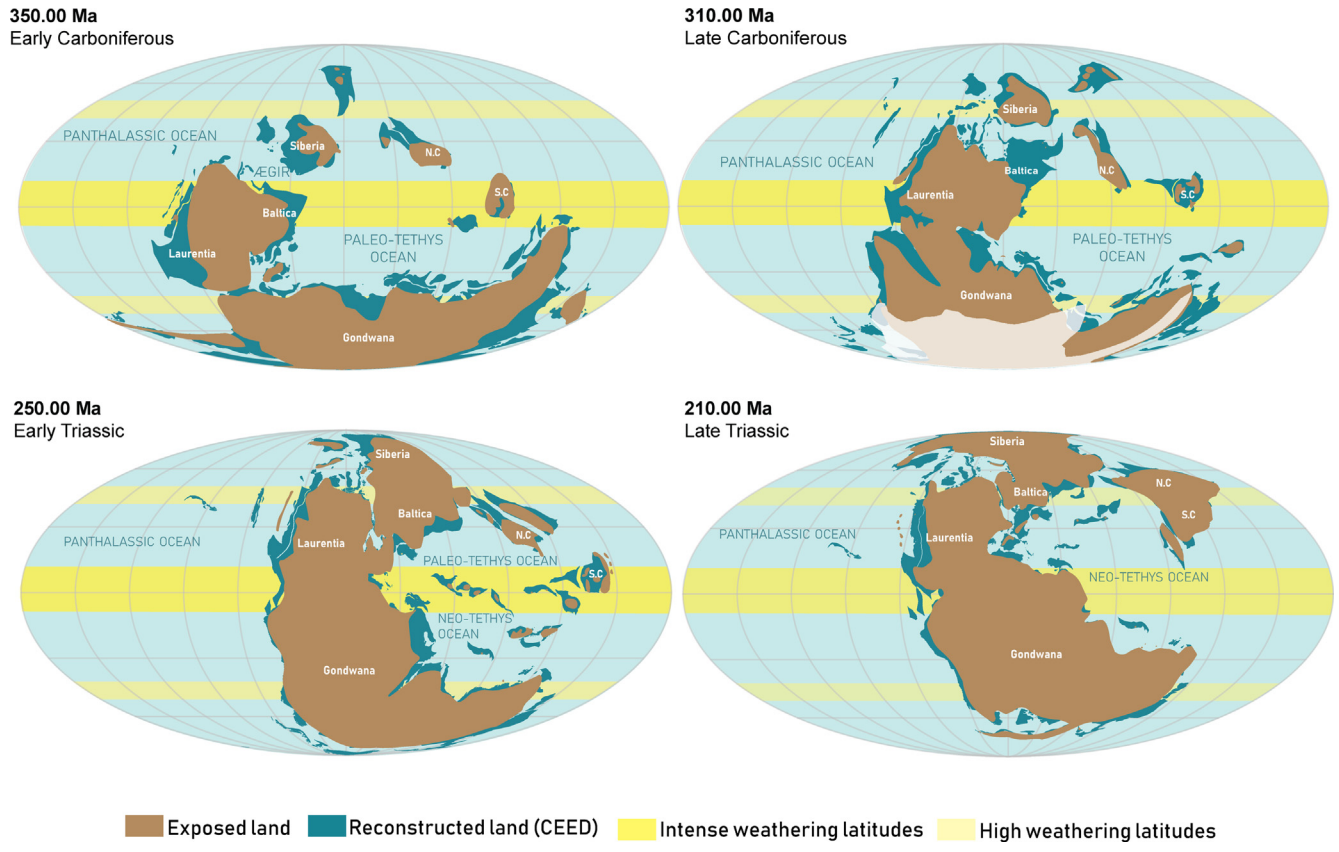


**Fig. 2** (*continued*)

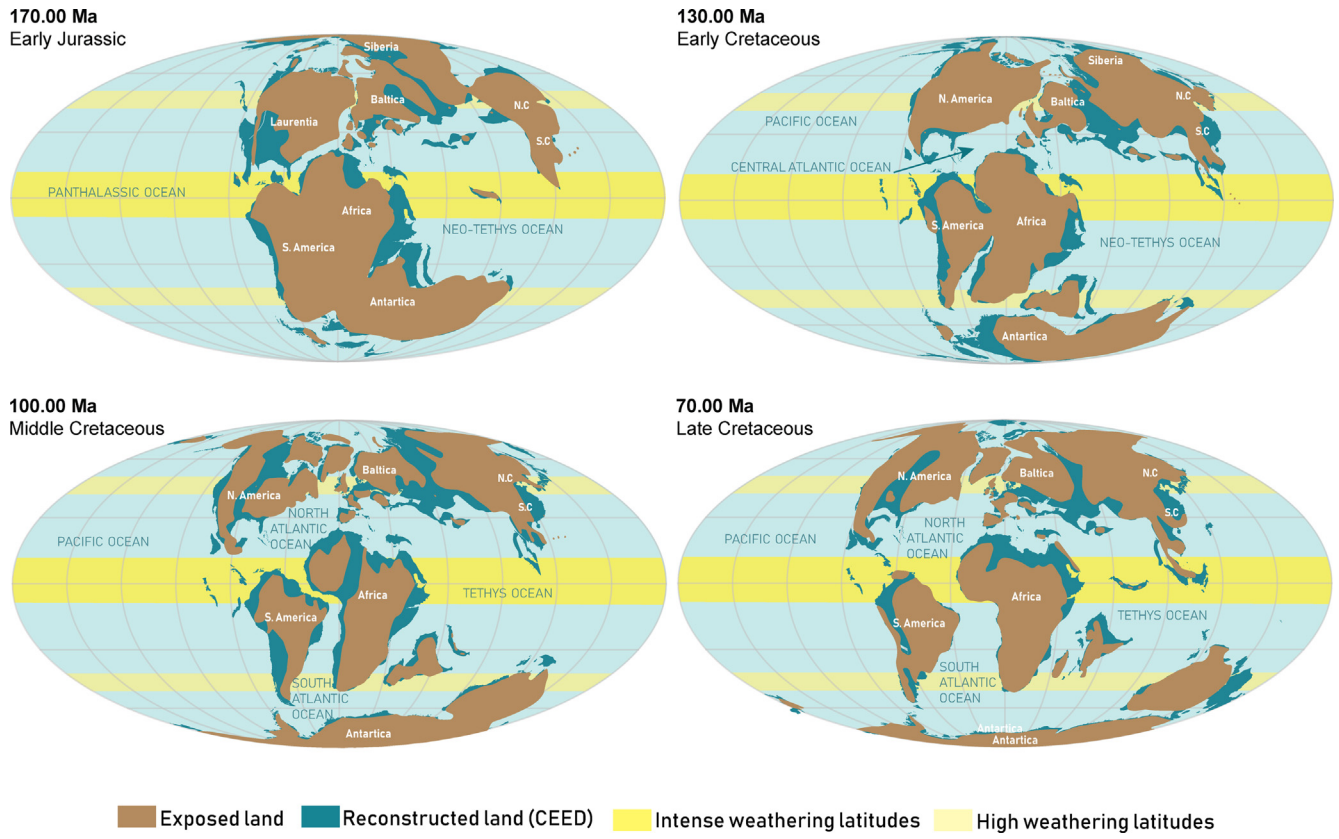


**Fig. 2** (*continued*)

**Table 1**
Overview of the longitude filter applied to the land area calculation to assess the effect of aridity associated with continentality during and following Pangea assembly and lasting beyond its break-up (270–110 Ma) on the ±10° latitude band.

| Time (Ma) | Filtered Longitudes | Exposed land Area ($10^6$.km$^2$) | Weighted Latitude | ABS Weighted Latitude | Land 10Deg ($10^6$.km$^2$) | Land 10Deg (%) |
|---|---|---|---|---|---|---|
| 270 | −45 to 20 | 113.79 | −16.07 | 38.06 | 7.36 | 6.47 |
| 260 | −45 to 20 | 128.79 | −10.70 | 35.88 | 7.84 | 6.09 |
| 250 | −30 to 5 | 128.27 | −8.15 | 36.57 | 7.62 | 5.94 |
| 240 | −30 to 0 | 133.74 | −7.22 | 36.31 | 9.77 | 7.30 |
| 230 | No filter | 134.58 | −5.52 | 36.88 | 16.34 | 12.14 |
| 220 | −30 to 15 | 130.59 | −3.52 | 36.27 | 7.29 | 5.58 |
| 210 | −30 to 15 | 138.10 | 3.04 | 35.14 | 8.28 | 6.00 |
| 200 | −35 to 30 | 131.17 | 11.79 | 37.27 | 4.73 | 3.61 |
| 190 | −35 to 30 | 132.88 | 8.73 | 36.58 | 7.13 | 5.37 |
| 180 | −35 to 30 | 136.99 | 6.07 | 36.97 | 7.01 | 5.12 |
| 170 | −35 to 30 | 120.71 | 3.71 | 37.87 | 5.16 | 4.28 |
| 160 | −35 to 5 | 106.97 | 6.99 | 37.68 | 5.24 | 4.90 |
| 150 | −35 to 10 | 115.08 | 4.06 | 38.50 | 6.34 | 5.51 |
| 140 | −35 to 10 | 119.59 | 4.57 | 39.37 | 6.97 | 5.83 |
| 130 | −35 to 10 | 114.85 | 6.25 | 39.94 | 6.11 | 5.32 |
| 120 | −40 to 10 | 105.28 | 12.43 | 40.08 | 5.56 | 5.28 |
| 110 | −40 to 10 | 115.45 | 10.22 | 40.56 | 6.80 | 5.89 |

silicate weathering, and hence lower $CO_2$ consumption (Michel et al., 2015; Mujal et al., 2018). We tested the effect of Pangea continentalisation on simulated $CO_2$ levels using GEOCARBSULFvolc in Section 5. For this, we reduce the availability of land to weathering by removing from our calculations longitude bands which include land exposed at ±10° latitudes (Table 1). The longitudes removed were so chosen according to the distribution of evaporites and coal.

We furthermore test two ways of evaluating weatherability (i.e. the potential of silicate weathering activity linked to paleogeography). We first consider weatherability restricted to the equatorial latitudes between 10°N and 10°S, corresponding to the region of most intense silicate weathering. We then consider a revised approach that also considers the exposed land between ±40 and 50°, in addition to the equatorial band. This revision is based on recent studies that have used the GEOCLIM model linking paleogeography and climate, which suggest that an important contribution to the global weatherability is provided by these mid-latitudes (Goddéris et al., 2014; Goddéris and Donnadieu, 2017; Hilley and Porder, 2008; Hartman and Richards, 2014). Note that because the continents were largely confined to the southern hemisphere in the early Paleozoic, estimates of exposed land area between ±40 and 50° latitude are exclusively derived from the southern hemisphere before 340 Ma (Fig. 3b). After Pangea formation, the mean continental latitude shows a systematic northward shift (Fig. 3a) and it is only from the Early to Mid-Jurassic that the amount of exposed land is similar for the northern and southern wet belts (Fig. 3b).

In Section 2.2.4, we compare reconstructions in terms of the amount of exposed land and in particular exposed land at latitudes with a high potential for silicate weathering (i.e high runoff and high temperature) for the different sets of reconstructions outlined in Section 2.1.1. Notably, these reconstructions do not consider relief, which greatly impacts weathering intensity, the development of thick regoliths that can limit silicate weathering efficiency (Ollier and Pain, 1996) or the occurrence of extensive lava blankets on the Earth's surface (following the emplacement of large igneous provinces) that can enhance silicate weathering. The estimation and implementation of such parameters into our paleogeographic model thus remains an important opportunity for future work.

### 2.2. Paleogeographic reconstructions and weatherability

#### 2.2.1. Early Paleozoic (Cambrian to Silurian)

In the early Paleozoic, nearly all the continents were located in the southern hemisphere (Fig. 2, plate 1: 520–420 Ma; Fig. 3a). Gondwana, the largest continental unit, which mostly formed in the late Neoproterozoic, stretched from the South Pole to the equator (western Australia) for most of the Paleozoic. Multiple other continents (including Baltica, Siberia, and North China) drifted progressively northward during the early Paleozoic, resulting in a string of independent landmasses along the equator in Ordovician and Silurian time. However, the then-northern part of Gondwana (western Australia) and Laurentia formed most of the exposed land at the equator for most of the early Paleozoic.

The northern hemisphere was dominated by the Panthalassic Ocean at this time, but another large ocean was present in the southern hemisphere, the Iapetus Ocean, which separated Laurentia from Baltica and Gondwana. The Iapetus had reached its zenith in the Cambrian and then progressively shrank during the Ordovician (Fig. 2, plate 1: 520–440 Ma) before disappearing entirely during the mid-Silurian collision of Baltica, Avalonia, and Laurentia that formed Laurussia (Fig. 2, plate 1: 420 Ma). Another important ocean, the Rheic Ocean, opened at ~480 Ma between Gondwana and Avalonia and remained an important ocean until ~320 Ma when Gondwana, Laurussia, and intervening terranes collided to form the supercontinent Pangea (Fig. 2, plate 2: 310 Ma).

The total exposed land area ($Land_{EXP\_TOTAL}$) was relatively small and stable during the early Paleozoic (Fig. 4a) but the exposed land within ±10° of the equator and between ±40 and 50°, i.e. latitudes with potentially high weatherability ($Land_{EXP\_Wtot}$), increased sharply between 510 and 460 Ma. A Phanerozoic maximum of 39% of the total exposed land (Fig. 4b, black curve) was reached by 460 Ma before declining again to only 20% by 380 Ma. Throughout this time, the latitudes between ±40–50° held a relatively low proportion of exposed land ($Land_{EXP\_W40/50}$, Fig. 4b, blue curve) compared with the remainder of the Phanerozoic, but also note that most continents were essentially located in only one hemisphere in the early Paleozoic (Fig. 3a). We observe particularly low values for $Land_{EXP\_W40/50}$ at 440 Ma, associated with a more than 5% drop from the Late Ordovician. Conversely, the area of exposed land within ±10° ($Land_{EXP\_W10}$) peaks sharply in the Middle-Late Ordovician, when it reached the highest theoretical tropical weathering contribution for the entire Phanerozoic (~23% of $Land_{EXP\_TOTAL}$) (Fig. 4b, red curve).

Some global sea-level curves suggest sea-levels increased during the early Paleozoic (peaking in the Late Ordovician) but this is not supported by our flooded land estimates (the inverse of the total exposed land), which are indicative of high but fluctuating sea-levels throughout the early and mid-Paleozoic (Fig. 4c). A low of about 23% of flooded land between 450 and 440 Ma coincides

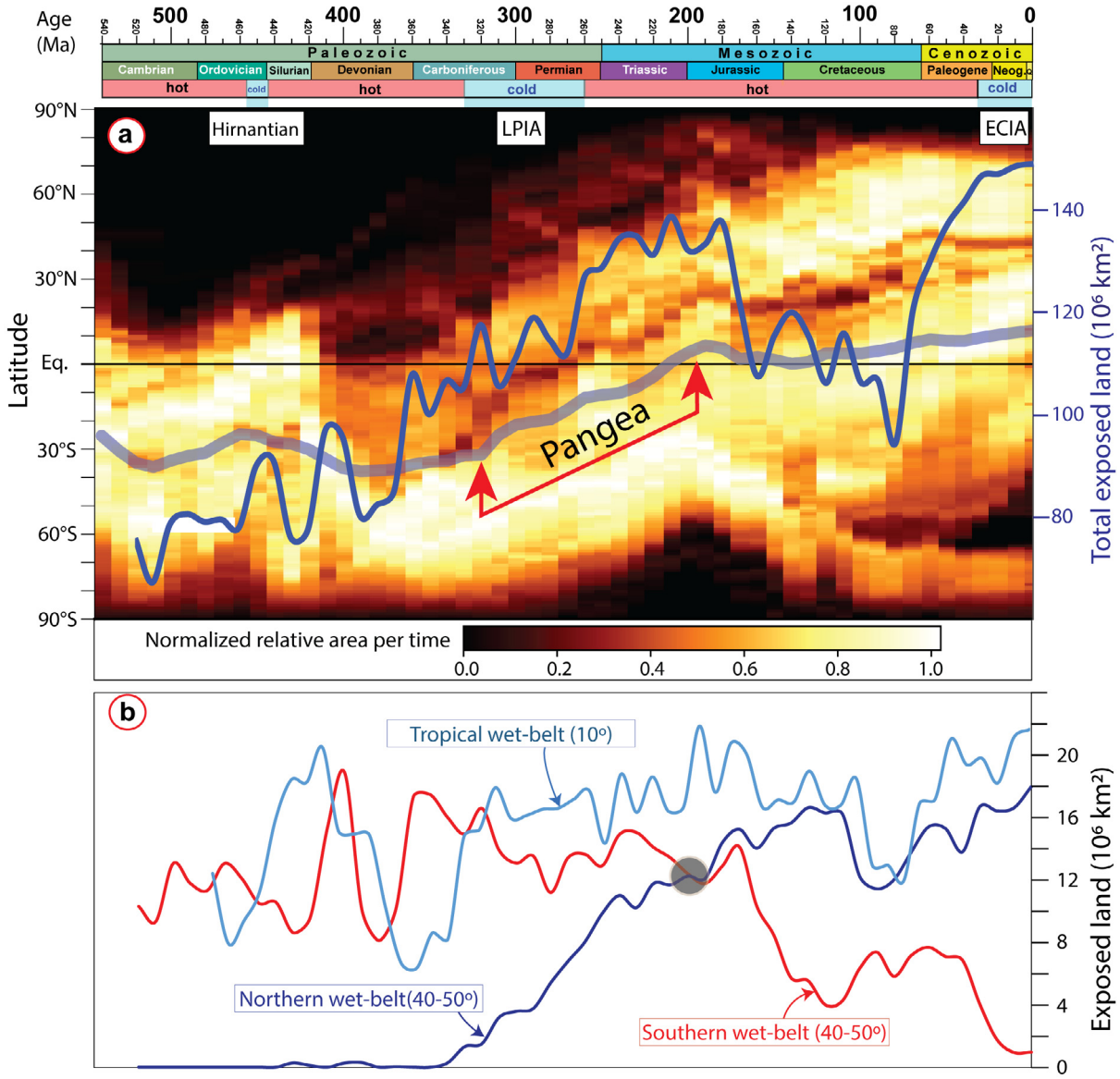


**Fig. 3.** (a) Phanerozoic timescale with greenhouse (hot) versus icehouse (cold) conditions. We consider three main icehouses (i.e Hirnantian, Late Paleozoic Ice age LPIA and End Cenozoic ice age ECIA). However, glacial deposits of latest Devonian, earliest Carboniferous age and the Middle-Late Jurassic probably witnessed episodes of cold climate (Dera et al., 2011). The heat-map shows the latitudinal distribution of continental area (lighter regions) as a function of time (Torsvik et al., 2020). The south polar areas remain dark even though it was occupied by continents several times in the past (including at present-day) because its area is small compared to the area of lower latitudes (the pole itself has no area). The thick grey curve shows the average continental paleolatitude (weighted by area) while the blue curve corresponds to the percentage of exposed land ($10^6$ km$^2$). Our model covers the period from 520 to 70 Ma followed by a revision of the model from Golonka et al. (2006; digitized in Heine et al., 2015) and Poblete et al. (2021) after 70 Ma. (b) Exposed land in the southern and northern hemisphere belts between 40 and 50° (wet belts) as well as within ±10°. Note the total lack of exposed land in the northern belt until the Carboniferous (~340 Ma) because all the continents were essentially located in the southern hemisphere during the early Paleozoic (panel (a)). During the Early Jurassic, the amount of exposed land is similar in the northern and southern wet belts and from the mid-Jurassic (~170 Ma); the northern wet belt starts to dominate over the southern wet belt. The grey circle highlights that 'cross-over'.

with the end-Ordovician (Hirnantian) icehouse, which may have lasted less than a million years (Cocks and Torsvik, 2020).

### 2.2.2. Late Paleozoic (Devonian to Permian)

By Early Devonian time, Gondwana had rotated such that South Africa occupied the South Pole, but the landmass still stretched from the pole to the equator (western Australia) and the largest part of its exposed land was located between 40 and 90°S (Fig. 2, Plate 1: 390 Ma). Siberia and North China continued drifting northward in Devonian time, vacating the equatorial positions they had in the Ordovician and Silurian, and reached latitudes of 10–40°N by the early Carboniferous (Fig. 2, Plate 2, 350 Ma). At 350 Ma, only the northern areas of Laurussia and South China were located between 10°N and 10°S. The Rheic Ocean between Laurussia and Gondwana had narrowed considerably by this time, and closed completely during the late Carboniferous formation of Pangea at 320 Ma (Fig. 2, plate 2, 310 Ma).

Pangea drifted slowly northwards (Fig. 3a) and brought the interior of the former Laurussia to an equatorial position by the late Carboniferous. By the beginning of the Permian (300 Ma), the continents were widely spread in latitude (stretching from the South Pole to at least 60°N) but restricted in longitude. Most

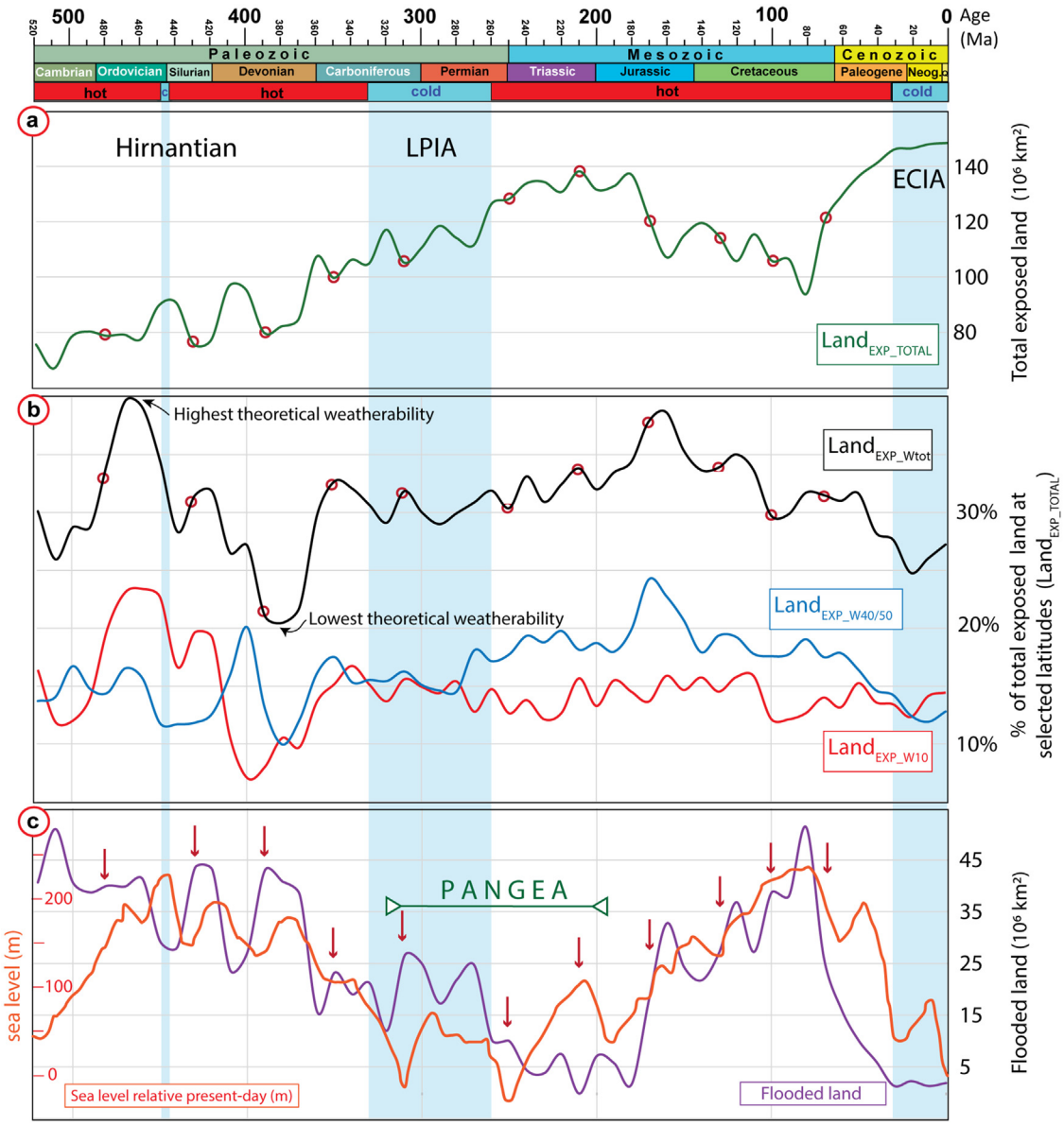


**Fig. 4.** Timescale with greenhouse (hot) versus icehouse (cold) conditions for the past 520 Myrs (see Fig. 3 caption) and (a) $Land_{EXP\_TOTAL}$ the total amount of exposed land (in millions of square kilometers: $10^6$ km$^2$). (b) Amount of exposed land for selected latitude bands of high theoretical weatherability, i.e. $Land_{EXP\_W10}$ at the tropics (±10°, red curve) and $Land_{EXP\_W40/50}$ at the northern and southern wet belts (±40–50°, blue curve) expressed as a percentage of total exposed land. The black curve, $Land_{EXP\_Wtot}$, is the total theoretical weatherability (combining ±10° and ±40–50°). (c) Relative sea-level curve (stratigraphic-based: Haq and Al-Qahtani 2005; Haq and Schutter 2008) compared with our estimates of flooded land (in millions of square kilometers: $10^6$ km$^2$). Flooded land (Total land - Exposed land) is scaled so that highs and lows mimic the global sea-level curve. The red arrows and red circles (panel a-b-c) represent times of reconstructed maps in Fig. 2. ECIA, End Cenozoic Ice Age; LPIA, Late Paleozoic Ice Age.

of the landmasses were located between 60°W and 60°E (Fig. 2, plate 2) and Pangea was surrounded on three sides by the large Panthalassic Ocean. To the east, Pangea was flanked by the wedge-shaped Paleotethys Ocean. Pangea never actually included all continental crust, and several Asian continental blocks were separated from the supercontinent by the Paleotethys (Fig. 2, plate 2: 310 Ma). In the early Permian, a string of terranes spalled off the northeastern margin of Gondwana, commencing the opening of the Neotethys Ocean, which then grew quite wide already by 250 Ma at the expense of a narrowing Paleotethys (Fig. 2, plate 2, 250 Ma).

During the Early Devonian, from 410 to 390 Ma, $Land_{EXP\_TOTAL}$ declined by ~17 mill. km$^2$ (15%) (Fig. 4a). At the same time, $Land_{EXP\_W10}$ dropped sharply and only 8% of $Land_{EXP\_TOTAL}$ occurred within those tropical latitudes from 400 to 390 Ma (Fig. 4b, red curve), reducing $Land_{EXP\_Wtot}$ to about 20% of $Land_{EXP\_TOTAL}$ and marking the lowest theoretical weatherability recorded for the entire Phanerozoic (Fig. 4b, black curve). In the Late Devonian $Land_{EXP\_TOTAL}$ increased again by more than 30 mill. km$^2$ (30%), reaching values above 112 mill. km$^2$ by 360 Ma, and then fluctuated around 115 mill. km$^2$ during the Carboniferous and Permian (Fig. 4a). $Land_{EXP\_Wtot}$ likewise climbed sharply in the Late Devonian to earliest Carboniferous and then fluctuated around 33% of $Land_{EXP\_TOTAL}$ for the remainder of the late Paleozoic (Fig. 4b). This marked increase in $Land_{EXP\_TOTAL}$ occurred seemingly in concert with decreasing sea-levels (Haq and Al-Qahtani, 2005; Haq and Schutter, 2008) which appears to have started 10 Myrs before, and is displayed by both our flooded land estimates and reconstructed sea-levels (Fig. 4c). The lowest sea-level (and

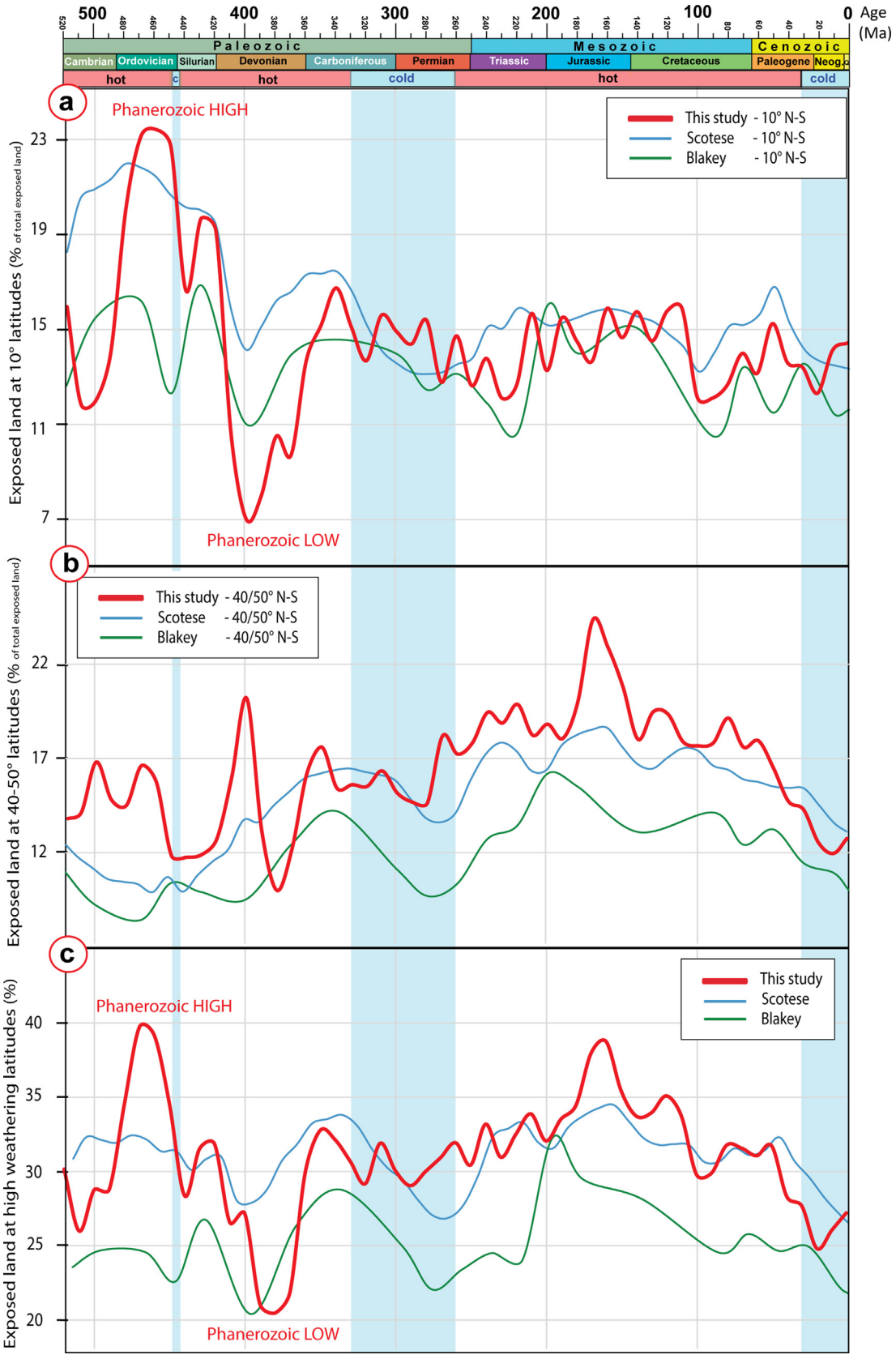


**Fig. 5.** Timescale with greenhouse (hot) versus icehouse (cold) conditions for the past 520 Myrs (see Fig. 3 caption) and (a) curves of exposed land at ±10° latitudes for three different reconstructions. The red curve displays the values estimated from our maps (as in Fig. 4b). The blue curve was *calculated* from the reconstructions of Scotese (2016) and the green curve was *estimated* from the reconstructions used in GEOCLIM (Blakey, 2009). (b) Same as in (a) but for latitudes ±40-50°. (c) Panels (a) and (b) combined, showing theoretical weathering activity in the tropics and the northern/southern wet belts.

correspondingly largest area of exposed land) from Paleozoic time was reached around 250 Ma, at the transition between the Paleozoic and Mesozoic eras.

*2.2.3. Mesozoic-Cenozoic*

Pangea drifted slowly but continuously northwards after it formed (Fig. 3a), and by the early Mesozoic the continents were spread in latitude from pole-to-pole (Fig. 2, plate 2, 250 Ma). Laurentia abandoned its equatorial position during the Triassic, whereas the northern part of Gondwana (North Africa and South America) migrated progressively into the equatorial realm. Three oceans dominated: the Panthalassic surrounded Pangea on three sides, whereas to the east the Paleotethys was shrinking and the Neotethys widening by the northwards movement of the Cimmerian and Sibumasu blocks (Fig. 2, plate 2, 250 Ma).

The most important phase of Pangea breakup started when the Central Atlantic Ocean opened in the Early Jurassic (~195 Ma), and by around 170 Ma the former Laurussia and Gondwana were separated by 250–400 km (Fig. 2, plate 3 170 Ma). Around that time, Gondwana also started to break up, leading to the separation of India, Madagascar, East Antarctica, and Australia from the rest of Gondwana (Fig. 2, Plate 3, 130 Ma). At the same time that Gondwana was disintegrating, Eurasia was amalgamating, and East Asia became fully part of Eurasia at around 130 Ma, when the opening of the South Atlantic started. By the Late Cretaceous, India had separated from Madagascar (Fig. 2, Plate 3, 70 Ma). During most of the Mesozoic, Africa and South America did not move much in latitude and their northern parts occupied the equatorial regions.

$Land_{EXP\_TOTAL}$ was high (~130 mill. $km^2$) from the late Permian to the mid-Jurassic but dramatically decreased between 180 and 160 Ma (Fig. 4a). However, $Land_{EXP\_Wtot}$ increased greatly during the late Paleozoic and early Mesozoic, reaching a peak at 160 Ma (Fig. 4b, black curve). During the Mesozoic, $Land_{EXP\_W10}$ showed less variability and fluctuated between 12% and 16% of $Land_{EXP\_TOTAL}$ (Fig. 4b, red curve). Conversely, $Land_{EXP\_W40/50}$ increased sharply between 190 and 170 Ma (blue curve in Fig. 4b), reaching the Phanerozoic maximum of around 22% of $Land_{EXP\_TOTAL}$ and producing the aforementioned peak in $Land_{EXP\_Wtot}$ (black curve in Fig. 4b). $Land_{EXP\_TOTAL}$ increased sharply (by ~60%) between 80 and 40 Ma before stabilizing close to present values for the rest of the Cenozoic (Fig. 4a). Conversely, $Land_{EXP\_Wtot}$ remained similar during the same period before decreasing between 50 and 20 Ma from 31 to 27% of $Land_{EXP\_TOTAL}$ (black curve in Fig. 4b).

Eustatic curves suggest that sea-level rose continuously over the Mesozoic (Haq and Al-Qahtani, 2005; Haq and Schutter, 2008), from the Phanerozoic low at 250 Ma to the Phanerozoic high in the Late Cretaceous (Fig. 4c). Sea-level then dropped precipitously in the latest Cretaceous and through to the present-day. These first-order eustatic trends (which are relatively well-defined for the Mesozoic-Cenozoic) are closely reflected by the flooded continental area curve derived from our exposed land maps.

*2.2.4. Comparison of reconstructed weatherability with other studies*

In Fig. 5 we have compared our estimated theoretical weatherability with those derived from the reconstructions of Blakey (2009) and Scotese (2016), and the diagram is separated into % exposed land at tropical latitudes (Fig. 5a), the northern/southern wet belts (Fig. 5b) and the total theoretical weatherability (Fig. 5c). In general, our model shows more variability than the two others do. In terms of total theoretical weatherability (Fig. 5c), our model shows a pronounced increase in the early Paleozoic, peaking in the Late Ordovician (40%), just before the Hirnantian glaciation. Although that peak in the total theoretical weatherability begins to abate before the onset of the Hirnantian glaciation, we note that the peak in the weatherability at 10° latitudes is sustained until the glaciation began (Fig. 5a). We consider this to reflect a meaningful link between that glacial event and weatherability, and more specifically the amount of land between the latitudes of 10°N and 10°S, where silicate weathering is about 20 times more intense than in the northern and southern wet belts (Goddéris et al., 2014). Enhanced continental weathering and $CO_2$ drawdown may therefore have been a contributing factor to the onset of that end-Ordovician glaciation (e.g., Kump et al., 1999; Goddéris et al., 2017). According to our model, this Late Ordovician peak of high theoretical weatherability is the highest recorded in the Phanerozoic, but it is absent in the two other models. This discrepancy is principally linked to the different positions of Siberia and Laurentia. In our reconstruction, Laurentia and Siberia but also the northern part of Baltica are included in the calculation of land available within the 10° latitudes whereas in reconstructions from Scotese and Blakey, they are above and below this 10° boundary.

During the Silurian and Devonian, there is a general (but oscillating) decrease to about 20% of all exposed land near the Devonian-Carboniferous boundary (~360 Ma), which is the lowest recorded for the Phanerozoic in our reconstruction. However, the three models show a drop immediately before in the ±10° latitudes triggering a general low for the reconstructions of Scotese and Blakey at 400 Ma. All three models then show a sharp increase in the total theoretical weatherability up to the mid-Carboniferous (Fig. 5a), with a peak in the ±10° latitudes just prior to the initiation of the Late Paleozoic Ice Age (LPIA). We consider the main LPIA phase to have lasted from 330 to ~275 Ma (Torsvik and Cocks, 2017) but minor glacial deposits can be tracked to about 260 Ma (e.g., Fielding et al., 2008; Montañez and Poulsen, 2013; Soreghan et al., 2019; Scotese et al., 2021). Both the Scotese and Blakey reconstructions display a drop in land at weatherability latitudes during the LPIA, whereas ours stay stable. The cause for this discrepancy is the difference in the modelled flooded area around Gondwana mostly in the latitudes 40-50°S and additionally over Laurussia and northern Gondwana for Scotese's reconstructions.

In the early Mesozoic, our model of total theoretical weatherability oscillates about a gradually increasing trend and ends with a pronounced peak in the Late Jurassic at 160 Ma (Fig. 5c, red curve). By comparison, the model of Scotese shows a more modest peak due to smaller fluctuations in the ±40–50°. However, the model of Blakey shows an earlier peak of total theroritical weatherability at 200 Ma before engaging a decrease lasting into the Cenozoic. This decrease is also observed in our reconstructions and Scotese's but from the mid-Jurassic.

Our model shows the highest variability during the early and mid-Paleozoic and is dominated by changes in exposed land at low latitudes (±10° red curve in Fig. 5a). The three models show very different characteristics but the reconstructions of Blakey (2009) show generally much less land in latitudes of potentially high weatherability compared to both our study and that of Scotese (2016) (Fig. 5c). This smaller proportion of land would lead to an underestimation of the silicate weathering potential and linked $CO_2$ sink in long-term climate models with the use of this model compared to Scotese's or ours. Generally, the large difference observed can be attributed to more flooding modelled on the coast of Gondwana as well as to the fact that many fewer islands and microcontinent are mapped in the work of Blakey (2009). However, this could also be due to the extrapolation necessary between the available maps of Blakey over the Phanerozoic which has a lower time resolution than the two other models discussed here.

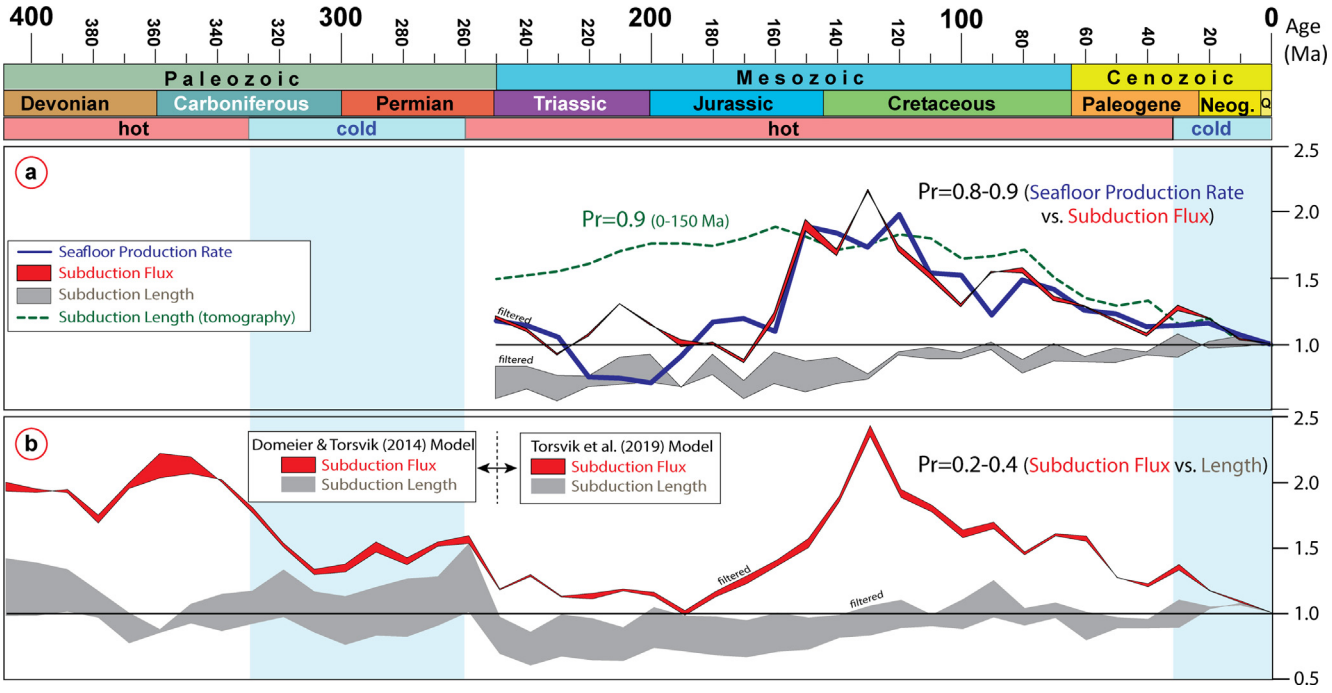


**Fig. 6.** Timescale with greenhouse (hot) versus icehouse (cold) conditions for the past 410 Myrs (see Fig. 3 caption). (a) Seafloor production rate from Coltice et al. (2013) (thick blue line) compared with our calculations of subduction lengths and fluxes from the same full-plate model (extension of the Seton et al. 2012 model) and subduction lengths from seismic tomography from van der Meer et al. (2014) (stippled green curve). Lengths and fluxes are shown with (upper part of shaded regions) and without filter cut-offs (see text). $P_r$ is the Pearson product-moment correlation coefficient (r), a dimensionless index ranging from −1.0 to 1.0 that reveals the extent of a linear relationship between two data sets. Seafloor production rate and subduction flux are well correlated for the past 160 Myrs with $P_r$ = 0.84 (unfiltered) and $P_r$ = 0.86 (filtered). For the past 250 Myrs $P_r$ = 0.76 (unfiltered) and $P_r$ = 0.79 (filtered). Notice that subduction lengths from this full-plate model show much less variability through time and are strikingly different from that of van der Meer et al. (2014). Van der Meer et al. (2014) and Coltice et al. (2013) curves compare well for the past 150 Myrs (P = 0.9). (*b*) Calculated subduction lengths and fluxes from Domeier & Torsvik (2014) and Torsvik et al. (2019; Model R) after 250 Ma. Subduction fluxes and lengths are non-correlated (P = 0.2–0.4 depending on filtering), implying that variation in fluxes depends on rate-variations and not lengths. Note a change in subduction lengths when switching between the two full-plate models.

## 3. Estimating degassing for long-term carbon models

The most important long-term solid Earth degassing occurs at continental arcs (including metamorphic decarbonation; Caldeira, 1992; Lee and Lackey 2015) and continental rifts, and to a lesser extent at island arcs and mid-ocean ridges (Lee et al., 2020). The global inputs from these non-plume carbon sources vary on geological timescales, predominantly due to changes in seafloor production/-consumption rates, and those rates are thus commonly employed in long-term $CO_2$ models as a proxy for degassing on geologic time scales (Berner, 2004; Berner, 2006; Royer et al., 2014; Goddéris and Donnadieu 2017; Mills et al., 2019). However, the specific estimates of those rates which have been widely employed in carbon cycle models are rather poorly constrained. The longest such proxy estimations have been derived from global sea-level fluctuations, given that changes in spreading rates (and thus mid-ocean ridge volume) are the most important driver of sea-level variations (Conrad, 2013). In long-term carbon cycle models, this parameterization of degassing is expressed as a time-dependent rate relative to present-day and dubbed $f_{SR}$ in GEOCARBSULFvolc. This term was originally defined as the '*seafloor creation rate*' but is now more generally treated as a proxy for rates of 'plate tectonic degassing', 'plate tectonic activity' or 'solid Earth degassing'. In accordance with its established use, we also adopt the term $f_{SR}$ to describe the degassing rate for long-term carbon models in this study.

### *3.1. Degassing since 250 Ma: Rates of crustal production and destruction vs. subduction lengths*

Back to 83 Ma, seafloor production rates can be calculated with a high degree of confidence from oceanic lithospheric age-grids derived from marine magnetic anomalies. Coltice et al. (2013) estimated Mesozoic-Cenozoic seafloor spreading rates ($f_{SR}$) by computing the 0–8 Myrs area from oceanic age-grids, as a moving average over the studied period, using an extension of the Seton et al. (2012) full-plate model. Normalized to today (=1), their estimation of $f_{SR}$ shows modern-day-like rates (within a factor of ±0.3) between 250 and 160 Ma, peak rates in the Late Jurassic-Early Cretaceous, and then, after 120 Ma, a gradual decline to modern-day rates (blue curve in Fig. 6a). In our models developed using GPlates, seafloor production rate and subduction flux must be equal due to the continental area being held fixed, and so any differences observed between them are due to the application of filters (see below). The subduction flux calculated from the same but unfiltered full-plate model used by Coltice et al. (2013), when compared against their seafloor production curve, yields a Pearson r-correlation ($P_r$) of 0.8 and 0.9 over the 0–250 Ma and 0–160 Ma range, respectively (where $P_r$ can range from −1 to 1 and $P_r$ = 1 denotes a perfect positive relationship). Although expected, this confirms that the rate of seafloor spreading and the subduction flux, as computed from the same model, closely correspond (Fig. 6a).

In contrast to the direct computation of $f_{SR}$ or the subduction flux, van der Meer et al. (2014) proposed that those fluxes could be more simply estimated from the time-dependent length of subduction zones. They mapped out the lateral extent of slabs from seismic tomography and then converted those to time-dependent subduction zone lengths using a geometrical correction based on a model of mantle density increasing with depth. By assuming the present-day, globally averaged rate of convergence (6 cm/yr., Schellart et al., 2008) to be constant through time, they estimated a normalized subduction flux that grossly matched the $f_{SR}$ curve of

Coltice et al. (2013) for the past 150 Ma ($P_r$ = 0.9, green stippled curve in Fig. 6a). However, if we repeat the same experiment on the plate model used by Coltice et al. (2013), we find that the time-dependent length of subduction zones shows very little variation with time (grey-shaded curves in Fig. 6a). This means that the variations earlier observed in the direct subduction flux calculation must be associated with changes to global convergence rates *and not subduction lengths* as suggested by van der Meer et al. (2014). By extension, this also means that variations in the rate of seafloor production are not simply due to changing ridge/rift lengths, but also to fluctuations in the globally averaged spreading rate. Many other studies employ normalized subduction lengths, continental rift lengths, or a hybrid combination of these two measures, to derive estimates of plate tectonic degassing (e.g. Mills et al. 2014, 2017), but the availability of full-plate models should now permit the community to work with convergence/divergence fluxes rather than boundary lengths. Interestingly, however, the coincidentally good correlation that van der Meer et al. (2014) observed between subduction lengths (assuming a constant average convergence rate) and the seafloor production rate curve of Coltice et al. (2013) back to 150 Ma implies there are important intra-oceanic subduction zones lengths which are missing (not represented) in the model used by Coltice et al. (2013).

To constrain the seafloor production rate through time we calculated the subduction flux directly from full-plate models, after some filtering (as described in Domeier et al., 2018) to remove artefacts associated with kinematic imperfections that are invariably present in full-plate models. For example, many transform boundaries are not perfect small-circles, and will therefore have some small component of transpression or transtension that is unlikely to have resulted in true subduction/spreading and should therefore be filtered out. Similarly, subduction zones and spreading centers may, for some short time-interval, exhibit unrealistic relative motions of small magnitude (e.g. divergence along a subduction zone). It is also important to average calculations over a time interval that is commensurate with the temporal resolution of the model itself. Our calculations were conducted in 10 Myr intervals and we imposed both orthogonal velocity (0–1 cm/yr.) and transform (0–20°) cut-off filters. However, it is worth noting that the subduction flux calculation is rather insensitive to even moderate filtering (as the filtered contributions are normally of very small magnitude), whereas the estimation of subduction lengths is much more sensitive to such filtering (Fig. 6a); incidentally, this is another reason why convergence/divergence fluxes present a better proxy for plate tectonic degassing.

### 3.2. Degassing since the Early Devonian (410 Ma) based on subduction fluxes

Investigation of a more recent full-plate model (Fig. 6b), corrected for published flaws in the reconstruction of the Pacific-Panthalassic (Torsvik et al., 2019), also demonstrates that the subduction flux and subduction lengths are uncorrelated ($P_r$ = 0.2–0.4, dependent on filtering). In fact, all published full-plate models (e.g., Torsvik et al. 2010; Seton et al. 2012; Matthews et al., 2016; Torsvik et al. 2019) that we have analysed show that the subduction flux is linked to variations in the average convergence rate whilst subduction lengths vary little with time (Fig. 6).

In Fig. 6b, subduction fluxes and lengths were calculated from two separate models, i.e. the Mesozoic-Cenozoic model of Torsvik et al. (2019), which is based on refinements of the Matthews et al. (2016) model for the past 250 Myrs, and the late Paleozoic model of Domeier and Torsvik (2014), which extends backwards from 250 to 410 Ma. The subduction flux curve is almost identical to that calculated in Domeier et al. (2018) and Torsvik et al. (2020). During the Devonian and early Carboniferous (410–340 Ma), the degassing rate was approximately twice that of present-day, and during the late Carboniferous and Permian, the degassing rate was approximately 1.5 times present-day rates. Interestingly, the mid-Carboniferous transition between those distinct rates (decline from >2 to <1.5 present-day rates) started shortly before the onset of the Late Paleozoic Ice Age (LPIA) at ~330 Ma, and continued until shortly after Pangea assembly at ~320 Ma. Following a mostly stable but slowly rising flux in the late Carboniferous and Permian (through the LPIA), there was a sharp drop at the Paleozoic-Mesozoic boundary, whereafter the subduction flux reached the lowest levels of the Phanerozoic (around 1.2) during the Triassic and Early Jurassic (Fig. 6b). Conspicuously, subduction lengths, which otherwise show very little variation with time, also show a pronounced drop near the Paleozoic-Mesozoic transition at around 250 Ma; we therefore suspect that this is an artefact of the switch between the different full-plate models. During the Jurassic, there was a systematic increase in the subduction flux, which peaked in the Early Cretaceous, at 130 Ma (Fig. 6b). Subsequently, in the remainder of the Mesozoic and Cenozoic, the subduction flux progressively waned toward modern times.

### 3.3. Constraining degassing in deep time: The use of detrital zircon ages

Plate models generally become increasingly uncertain with increasing time. Prior to Jurassic time the reconstructed oceanic lithosphere is entirely synthetic (Torsvik et al., 2010) and before Pangea formed (~320 Ma) the longitudinal location of the continents is not strictly known. In recent years, a method using deep mantle structures as a reference frame for surface movements to resolve paleolongitude has emerged (Torsvik et al., 2014). That method is exploited in the reconstructions herein, as well as in the full-plate model of Domeier and Torsvik (2014), but the validity of this method in deep time is debated. It is therefore prudent to seek additional, complementary methods that can quantify the subduction flux and thus solid Earth degassing in deep time. One exotic pathway could be to consider the history of geomagnetic reversals, which may be tied to the global subduction budget since subducted slabs affect the core-mantle boundary heat flow and thus the geodynamo (Hounslow et al. 2018). However, the history of geomagnetic polarity is not generally well-defined prior to the Permian, and the specifics of this relationship are still poorly resolved. Another more promising pathway is to consider the age-frequency relationship of detrital zircons, the production of which may mimic true variations in the subduction flux, both regionally and globally (Domeier et al., 2018). Indeed, the use of zircon abundances to infer changes in plate tectonic degassing and greenhouse vs. icehouse climates has already been pioneered by McKenzie et al. (2016).

Here we further explore the use of detrital zircon age distributions to estimate the subduction flux. To accomplish this we queried the large global zircon database of Voice et al. (2011; V11). Although there are larger, more recent databases available (e.g. Puetz et al. 2018), we elected to use V11 because it includes convenient tectonic environment metadata tags, which make it easier to extract zircon ages that can be linked to arc environments. V11 and the database of Puetz et al. (2018), however, are broadly similar, with highs and lows in zircon abundance observed at approximately the same ages throughout Earth history (see also Domeier et al. 2018), and they yield a $P_r$ correlation of 0.92 over the entire studied age range.

The V11 database was first quality-filtered to eliminate imprecise/poor data, which was achieved by removing: *(i)* all results associated with a one-sigma ($1\sigma$) level error that exceeded 20% of the best-estimated age of the grain, *(ii)* all results with a best-estimated age less than the youngest-estimated depositional age

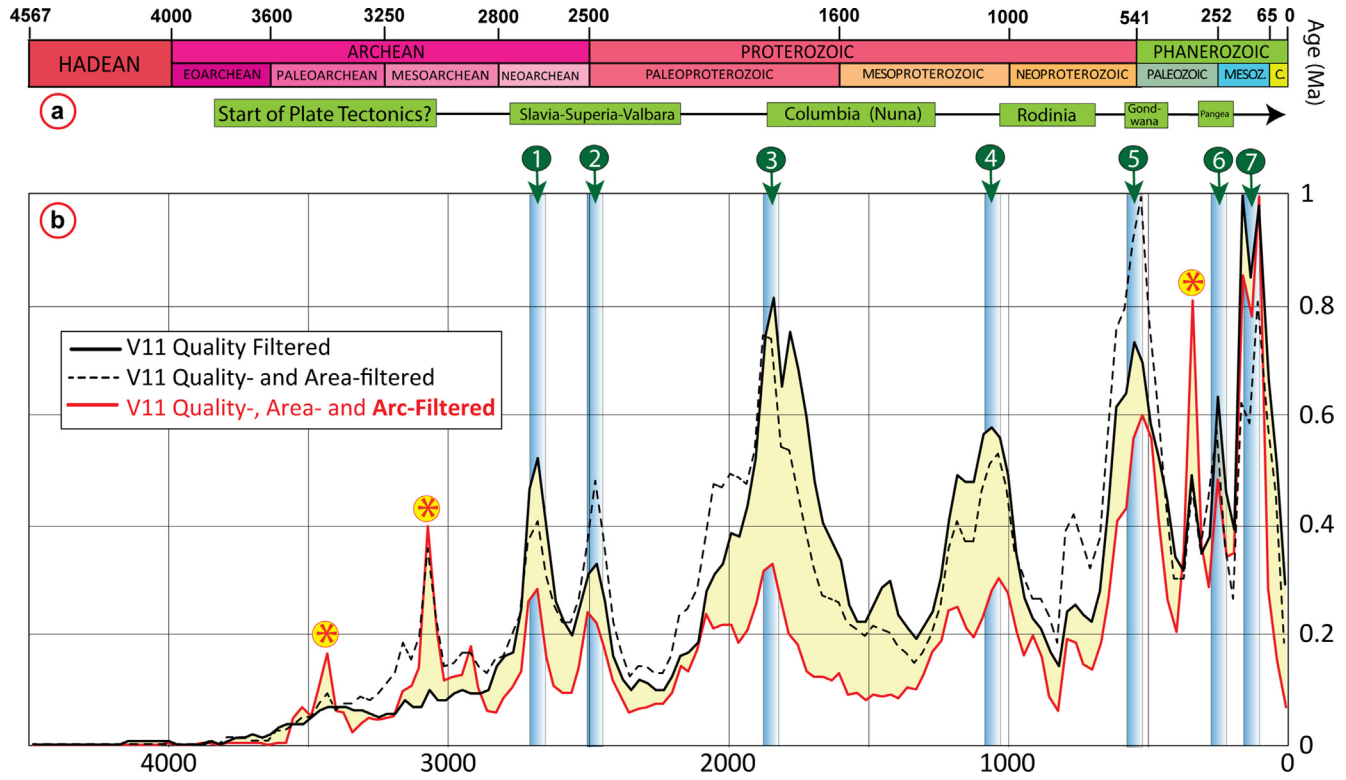


**Fig. 7.** (a) Timescale over the past 4,500 Myrs and the estimated assembly/dispersal of super-cratons/superterranes (Slavia, Superia, Valbara, and Gondwana) and supercontinents (Columbia, Rodinia, and Pangea; after Torsvik & Cocks, 2017). Note that the main phase of Gondwana took place during late Neoproterozoic-early Paleozoic times but the core of this superterrane lasted until merging with Laurussia to form Pangea at around 320 Ma. (b) Normalized zircon age frequency (Voice et al. 2011; V11), *first* quality-filtered (black curve), *then* area-filtered (stippled black curve), and *finally* arc-filtered (red curve) (see text for details). The quality-filtered curve shows seven major peaks since the late Archean. Those peaks are also seen after area filtering but the main Cretaceous quality-filtered peak (peak 6) is shifted to the early Cambrian (540 Ma, i.e. during Gondwana formation). There is also an additional peak in the early Mesoarchean. The latter is also pronounced after arc filtering that also shows a minor peak in the Paleoarchean and an additional peak at around 350 Ma (prior to Pangea assembly). Yellow shading shows the difference between quality-filtered and area + arc-filtered curves.

of the strata minus the one-sigma error of the grain age, and *(iii)* ages older than the age of the solar system and Earth (>4567 Ma). These filtering steps reduced the total number of zircon ages by ~3% (leaving 186,812 entries) but did not result in a significant alteration of the shape of the age distribution. This post-filtering distribution (shown using 30 Myr bins in Fig. 7) is similar to that of Domeier et al. (2018) except that ages in excess of 3.6 Ga were excluded from their histograms. There are seven main age-frequency peaks, the two oldest (peaks 1 and 2) are contemporaneous with some major craton interactions starting at ~2.7 Ga, whilst peaks 3 to 5 broadly coincide with the assembly of the two first supercontinents—Columbia (1.9–1.8 Ga) and Rodinia (1.1–1.0 Ga)—and the formation of the large landmass of Gondwana (peak 5). In Phanerozoic time, one peak is approximately coincident with Pangea formation, but the largest age-frequency peak is observed in the Early Cretaceous, when Pangea was rapidly disintegrating (peak 7 in Fig. 7).

We also applied an area-scaling to the V11 dataset in an attempt to compensate for the very uneven geographic distribution of the zircon sampling. The area scaling adds more weight to under-sampled regions (or equivalently, reduces the weight of over-sampled regions). The effect of this area scaling (stippled curve in Fig. 7) is significant, especially in reducing the amplitude of the peaks of the last ~300 Myr (mostly coming from North America) and in increasing some of the older peaks; for example, the peak around 540 Ma coincident with Gondwana assembly.

A third filtering step was applied to reduce the signal from non-arc related contributions. All entries in V11 are tagged with a tectonic environment, and of the eight varieties, three environments (fore-, back- and retro-arc basins) are directly associated with arc volcanism. We therefore removed all other entries from the quality- and area-filtered version of the dataset (Fig. 7), leaving 47,231 entries. There are some notable caveats to be mentioned with regard to this last filter. First, in addition to igneous rocks, both sedimentary and metamorphic rocks can exist in arc-related environments, and thus recycled zircons are not entirely stricken from the dataset by this filter. Second, most 'arc-related' zircons now exist in non-arc-related environments (e.g., recycled into passive margin sediments). We note that the general shape of the arc-, quality- and area-filtered V11 curves remain similar, but two new peaks appear in the Precambrian after application of the last filter. There is also a notable augmentation of a formerly subtle inflection in the age-frequency curve at around 350 Ma (red curve in Fig. 7). Finally, we de-trended the age-frequency curve, assuming the background monotonic decrease in zircon frequency with increasing age to be a reflection of preservation issues, but the slope (−0.0004) over the past 800 Ma is minor, and consequently the de-trended and non-trended curves are almost identical. In Fig. 7, the zircon age-frequency histograms resulting from these various filtering steps are compared after being scaled to their highest individual peaks.

As observed by Hounslow et al. (2018), we find that the shape of our final V11 zircon age-frequency distribution resembles the directly computed subduction flux of the last 410 Ma, with a minor temporal offset (Fig. 8a; see also Domeier et al. 2018). Specifically, since the start of the Phanerozoic, the zircon age-frequency distribution shows five main peaks. The oldest, in the Cambrian at around 520 Ma (P#1, Fig. 8a), is too old to be compared against

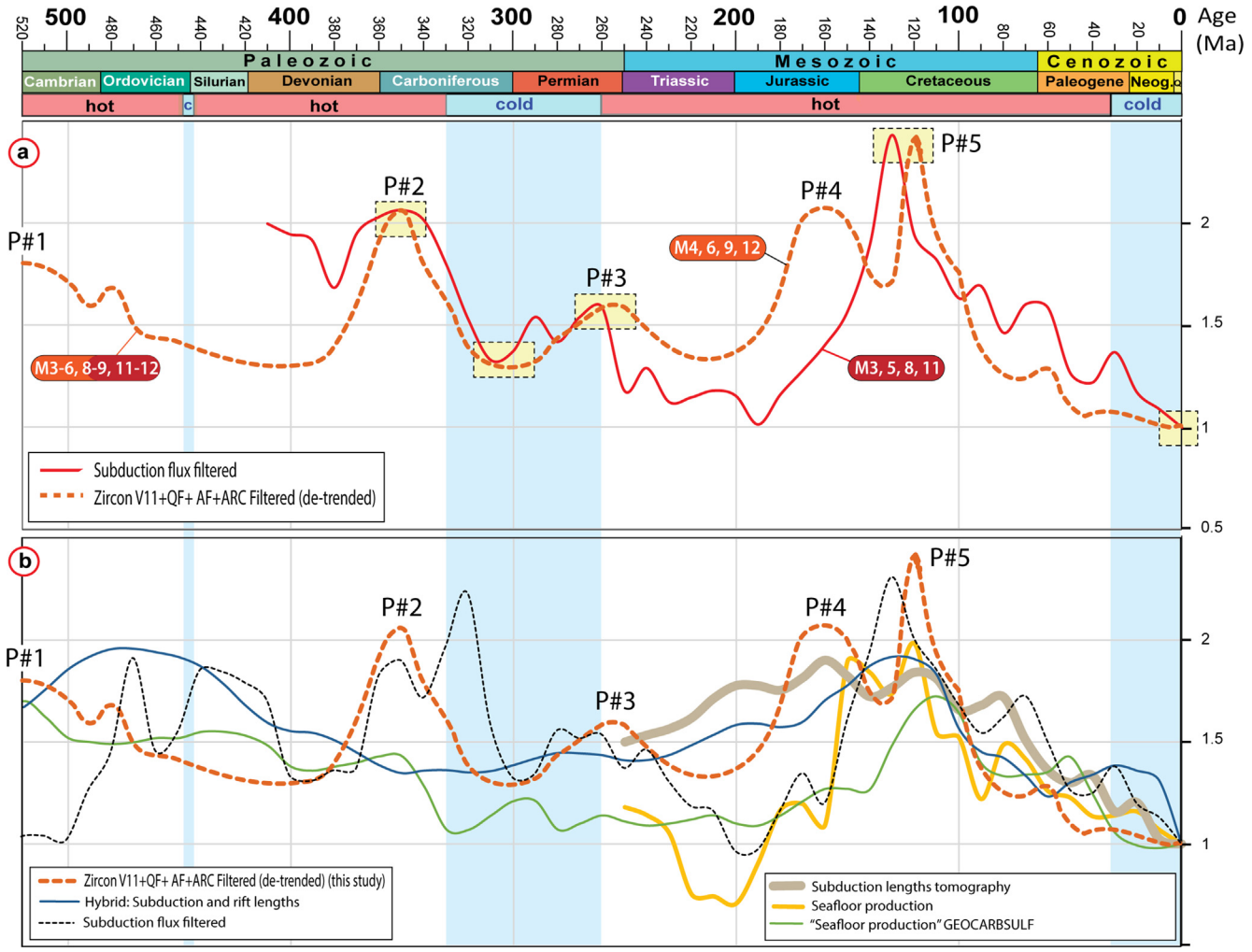


**Fig. 8.** Timescale with greenhouse (hot) versus icehouse (cold) conditions for the past 520 Myrs (see Fig. 3 caption) and (a) revised $f_{SR}$ (this study) based on two degassing proxies, i.e. subduction flux from full-plate models (red curve) and scaled arc-zircons (stippled orange). Subduction flux (filtered) for the past 410 Myrs (0–250 Ma also shown in Fig. 7b) shows peaks in the early Carboniferous (340–360 Ma), late Permian (~260 Ma), and the Early Cretaceous (~130 Ma). Two lows (late Carboniferous and Recent times) coincide with icehouse conditions whilst a third low in subduction flux (~190 Ma) coincides with greenhouse conditions. Subduction flux is compared with the frequency of arc-related zircons (Voice et al. 2011, V11) that have been quality- and area-filtered. Assuming that the general trend of decreasing zircon frequencies through time may reflect real preservation problems we have de-trended (with very little effect) the arc-zircons curve for the past 800 Myrs (slope = −0.004). The arc-zircon curve was then *rescaled* to the subduction flux by fitting three peaks of approximately the same age (P#2, #3, and #5) and a Permo-Carboniferous low at around 300 Ma (yellow boxes). The zircon data were binned in 10 Myrs intervals. Values for present-day and 10 Ma were set equal to unity (=today). The M# labels refer to the models including the presented proxy for their simulations (see Table 2). (b) Comparison of scaled arc-zircons and other proxies for $f_{SR}$. Only three have been estimated for the entire Phanerozoic. The "seafloor production" curve of Berner (2004) from sea level inversion, is the default $f_{SR}$ in GEOCARBSULF(volc) whereas the hybrid curve of Mills et al. (2019) is the default in COPSE. For comparison we also plotted the subduction fluxes calculated from the full-plate model of Merdith et al. (2021) (stippled black curve).

the subduction flux curve, but a second peak observed in the early Carboniferous (P#2) and a smaller high in the late Permian (P#3) are both comparable to similar inflections in the subduction flux. A fourth peak observed in the zircon age-frequency distribution, in the Middle Jurassic (P#4), is not evident in our subduction flux, whilst the fifth peak (P#5 at 120 Ma, Fig. 8a) is observed about 10 Myrs after the subduction flux peak. Both peaks P#3, P#5, and a Permo-Carboniferous low show an offset of about 10–15 Myrs, which is similar to the temporal offsets found by Domeier et al. (2018), who conducted comparisons between zircon age-frequency distributions and the subduction flux on a regional scale.

Given the first-order correspondence of these independent datasets since the late Paleozoic, we postulate that the zircon age-frequency distributions of earlier time may present a useful subduction flux proxy (and thus a proxy for 'plate tectonic activity' or solid Earth degassing). However, to use the arc-zircon record as a potential measure of the relative subduction flux we must re-scale the arc-filtered zircon curve to the subduction flux curve since 410 Ma. We did this by fitting *(i)* early Carboniferous to Early Triassic highs and lows (360–250 Ma; yellow box in Fig. 8a), *(ii)* Early Cretaceous peaks at 130 and 115 Ma, and *(iii)* normalizing the zircon distribution by the youngest value (giving the youngest bin a value of 1). The latter is important because the zircons generated by recent-to-ongoing arc-activity have mostly not been accounted for, since the formation of a zircon, and subsequent uplift and exposure of its host lag behind ongoing subduction. Thus, one cannot assign present-day or very recent zircon counts as representative of today.

## 4. Revision of paleogeographic and degassing input parameters in GEOCARBSULFvolc

GEOCARBSULFvolc is a popular long-term carbon and sulfur cycle model (Berner, 2006). This model estimates atmospheric $CO_2$ and $O_2$ levels by reconstructing the important long-term

sources and sinks through time (Royer et al., 2014; Berner 2004, 2006). If sources are defined mostly through the degassing input (translated by $f_{SR}$), the sinks are more highly parameterized and are mostly represented by silicate weathering intensity and carbon burial through time. The silicate weathering activity is constrained by different forcings affecting its rate, such as land plant evolution (translated by LIFE, GYM and FERT parameters), land temperature (GEOG), runoff ($f_D$), effect of relief on the weathering rate ($f_R$), and is scaled in its expression by the land area parameters that we revise here. The GEOCARBSULFvolc model has 68 input parameters, 12 of which are time-dependent. Our study concerns three of these time-dependent variables, namely (1) $f_A$, the exposed land area, (2) $f_{AW}\_f_A$, the fraction of exposed land undergoing chemical weathering and (3) $f_{SR}$, the seafloor creation rate (=subduction flux), as discussed above. $f_A$ is expressed as the time-dependent total exposed land area relative to the presently exposed land area, for which we use a value of $149 \times 10^6$ km$^2$ in Eq. (1):

$$f_A = \frac{exposed\ \ land_t}{149 * 10^6} \quad (1)$$

For $f_{AW}\_f_A$ we estimate the amount of exposed land at latitudes with a high theoretical weatherability through time. We consider both ±10° only (called $f_{AW10}\_f_A$), and ±10° plus ±40–50° (called $f_{AW}\_f_A$), and its expression can be written as in Eq. (2):

$$f_{AW}\_f_A = \frac{\left(\frac{exposed\ \ land\ \ at\ \ high\ \ weathering\ \ latitudes_t}{total\ \ exposed\ \ land_t}\right)}{\left(\frac{exposed\ \ land\ \ at\ \ high\ \ weathering\ \ latitudes_{t=0}}{total\ \ exposed\ \ land_{t=0}}\right)} \quad (2)$$

The considered present-day ratio values are 0.26 for $f_{AW}\_f_A$ and 0.145 for $f_{AW10}\_f_A$. Those values are based on our paleogeographic model at time zero.

This parameter was first introduced by Royer et al. (2014) in view to depict more realistically the expression of chemical weathering in the model. The resulting "Goddéris" version of the parameter in Royer et al. (2014) uses simulations from GEOCLIM (Goddéris et al., 2012) to select the fraction of land area that had non-zero runoff (based on paleoreconstructions of land and topography) to calculate $f_{AW}\_f_A$. If this version of the parameter is valuable progress for the model, as it allows to exclude cold and

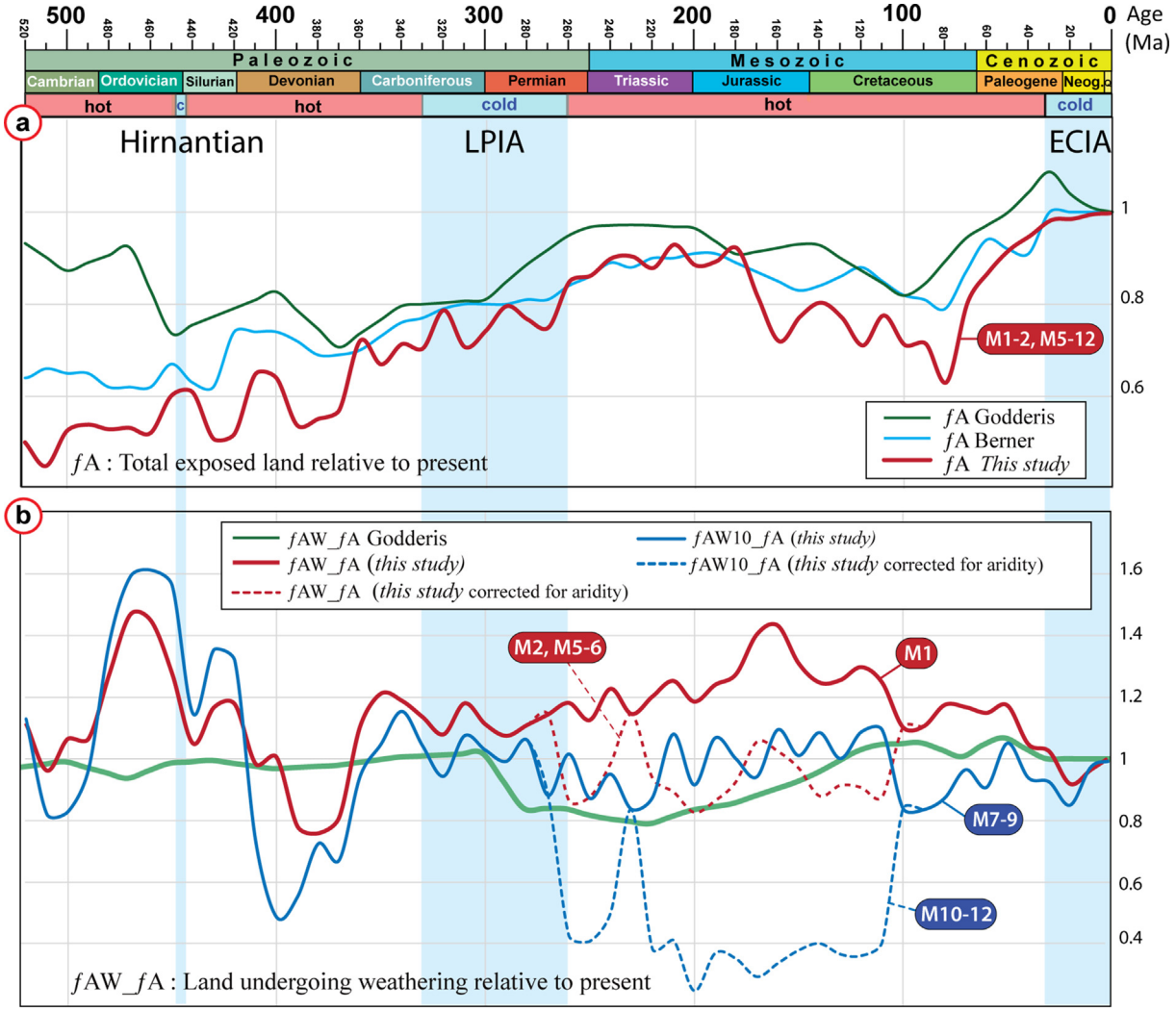


**Fig. 9.** Timescale with greenhouse (hot) versus icehouse (cold) conditions for the past 520 Myrs (see Fig. 3 caption). (a) Revised $f_A$ (this study) compared with the two different options available in GEOCARBSULFvolc, i.e. Berner or Goddéris weathering parameters (Royer et al. 2014). (b) Revised $f_{AW\text{-}fA}$ (this study) compared with the Goddéris values in GEOCARBSULFvolc (Berner is set to 1 for the entire period). Two considerations of weatherability are here tested. The red curve corresponds to the total weatherability formed at latitudes of ±10° & ±40–50°, whereas the red curve displays the weatherability only at ±10° ($f_{AW10}$-$f_A$). From the mid-late Permian to the mid-Cretaceous, climate gradients were much different from today, with arid tropical areas; we have excluded those areas between 280 and 100 Ma, and the resultant $f_{AW}$-$f_A$ is shown by the stippled curves for both definitions of weatherability considered. All values for the parameters are presented in the Table S1 of the supplementary data 2. The M# labels refer to the models including the proxy selected in their simulations. A list of the models is presented in Table 2. ECIA, End Cenozoic Ice Age; LPIA, Late Paleozoic Ice Age.

dry environments from the calculation of weathering, it also creates some limitations. The coarse grid size used in the model from Goddéris et al. (2012) retricts the integration of the effect of microcontinents and volcanic islands in their climatic simulations and linked weathering calculation. Those small land areas are particularly important in the early Paleozoic for example. Moreover, the input for those simulations comprised only 22 maps used to represent the entire Phanerozoic, and thus large extrapolations were required. Furthermore, the land availability was overestimated and the runoff simulations were based on extremely poorly constrained paleotopography, leading to an increased (and highly uncertain) silicate weathering activity throughout the Phanerozoic.

Here, we used a more simplified definition of land availability through time by extracting the amount of land, including some microcontinents and islands, located in specific latitudes. This assumes that climate gradients are constant through geological time (e.g. wet and warm tropics) and that runoff is globally similar to that determined from GEOCLIM reconstructions, both of which are important limitations. However, the distinct advantage of this approach is that we are able to evaluate the underlying effects of paleogeography, which is relatively well-constrained (and further improved herein), independently of the significant but poorly constrained effects of changing relief and climate zonation (which are ultimately tied back to paleogeography). In other words, we seek an improved understanding of the relationship between well-determined base paleogeography and climate, providing a framework on which progressively more sophisticated analyses can build.

### 4.1. Revision of $f_A$ and $f_{AW\_fA}$

The GEOCARBSULFvolc model can be operated in two different modes in the most recent R-code: '*Berner*' and '*Goddéris*' (Royer et al., 2014). These modes have different weathering-related parameters, based on Berner (2004) and Goddéris et al. (2014), respectively. In Fig. 9a, we compare the *'Goddéris'* and *'Berner'* values for $f_A$ against our own (calculated from the total land area estimations and their fluctuations as detailed in Section 2). There are broad similarities from the early Carboniferous to the Early Jurassic (about 360–180 Ma) but there are relatively large differences in the early and mid-Paleozoic (520–360 Ma) and during the Late Jurassic and Cretaceous. It is also noteworthy that the $f_A$ values of *'Goddéris'* are systematically higher than the *'Berner'* values. All models hold similar levels during and directly following the LPIA as the low sea-level maximized the amount of exposed land (Figs. 9a & 4c).

Our estimates of $f_{AW\_fA}$, calculated from the estimations of exposed land area in selected latitude bands (Section 2) extend from 520 Ma (we use the original GEOCARBSULFvolc parameters from 570 to 520 Ma) (Fig. 9b). They are very different from '*Goddéris*' (green curve in Fig. 9b), as well as the '*Berner*' model, which holds $f_{AW\_fA}$ always = 1 (Fig. 9b; Supplementary data 2, Table S1). In the model of '*Goddéris*', $f_{AW\_fA}$ shows hardly any differences from the Cambrian to the late Carboniferous, whereas our estimation exhibits strong fluctuations, including both the Phanerozoic maximum and minimum. Near the Carboniferous-Permian boundary, during the LPIA, the $f_{AW\_fA}$ of '*Goddéris*' exhibits a distinct reduction to about 0.8 that lasted until the Early Jurassic. By contrast our estimation of $f_{AW\_fA}$ exhibits a gradual increase

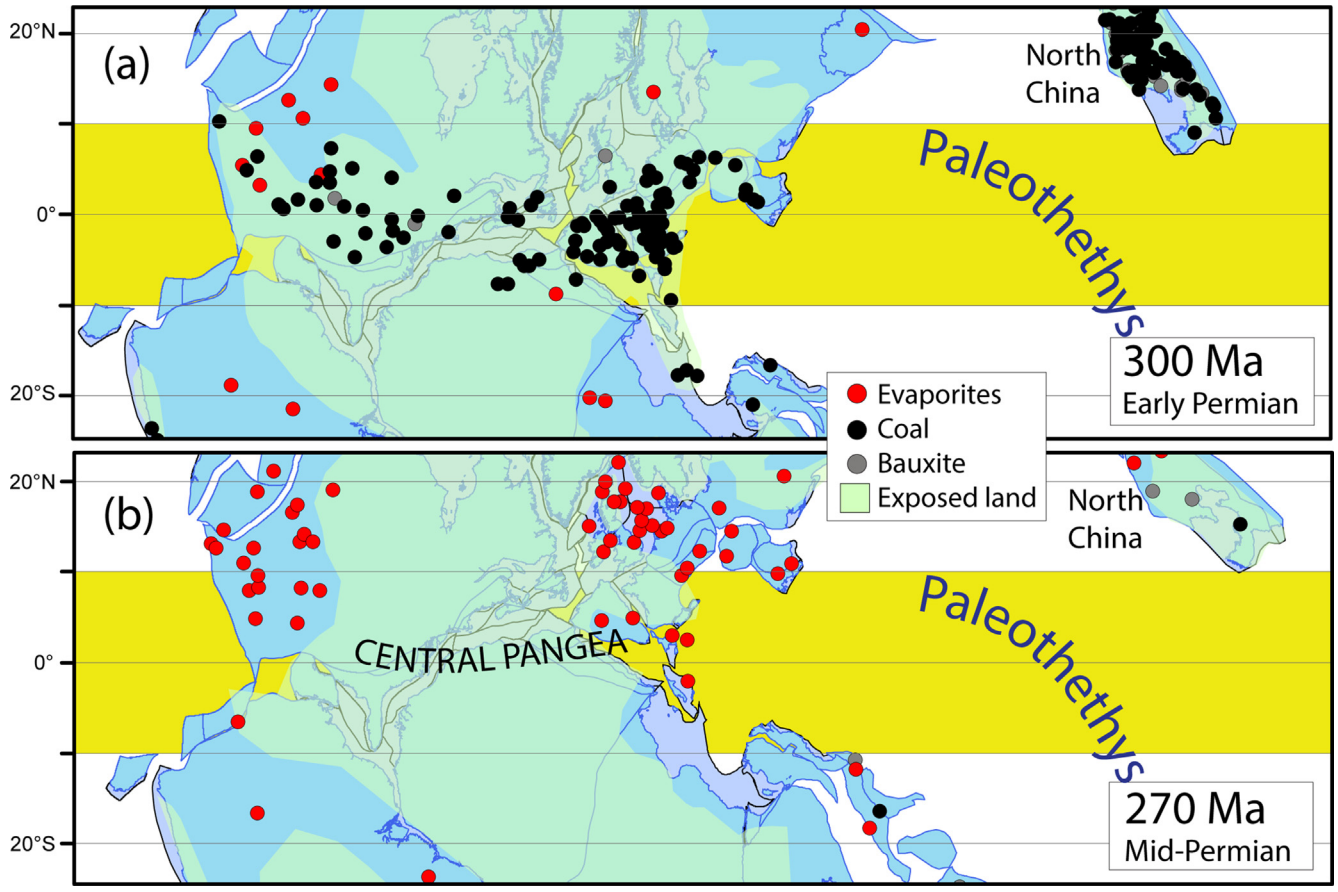


**Fig. 10.** Reconstruction of Central Pangea and the western parts of the Paleotethys together with exposed land and the distribution of evaporites, coal, and bauxite at (a) 300 Ma and (b) 270 Ma. Both reconstructions are in the paleomagnetic reference frame and the theoretical low-latitude belt of high weatherability is shaded yellow (±10°).

throughout that interval, and thus the estimates of $f_{AW}$_$f_A$ by '*Goddéris*' are consistently lower than ours from the early Permian to the mid-Cretaceous (compare green and red solid curve in Fig. 9b). From ~100 Ma to present-day the curves are in closer agreement.

Paleogeographic biome maps for the early phase of the LPIA and Pangea assembly (Fig. 10a) suggest that climate gradients then were grossly similar to those of the present-day (Torsvik and Cocks, 2017). However, as the Pangean climate aridified in response to growing continentality, the rain forests collapsed and were eventually replaced by seasonally dry biomes in the early Permian (Sahney et al. 2010). Subsequently, in middle-late Permian time, an expansive arid region extended across much of Pangea (Fig. 10b), spanning both northern and southern latitudes, and crossing both the Americas and Europe (Boucot et al. 2013; Torsvik and Cocks, 2017; Torsvik et al. 2020). Low global climatic gradients and a low latitude arid region traversing most of central Pangea characterized the Triassic and Jurassic, but even long after Pangea breakup, many equatorial regions appeared arid until about 100 Ma.

To account for the low climate gradients between 270 and 110 Ma, revised calculations of exposed land at high weathering latitudes were made by removing exposed land polygons where paleoclimate indicators (evaporites) suggest low-latitude (±10° arid conditions (Table 1). This reduces $f_{AW}$_$f_A$ considerably (stippled red curve in Fig. 9b), and brings it into closer agreement with the '*Goddéris*' curve (green line in Fig. 9b).

Considering that numerical simulations suggest that $CO_2$ consumption by silicate weathering in the tropics is perhaps 20 times higher than that achieved by the northern/southern wet belts (Goddéris et al. 2014), we also explore the use of $f_{AW10}$_$f_A$ (Fig. 9b blue curves). This has some important consequences: $f_{AW10}$_$f_A$ is about 1.6 times higher than present-day values in the mid-Late Ordovician compared to 1.45 for $f_{AW}$_$f_A$. The latter is already the highest potential $CO_2$ sink by silicate weathering observed from the entire Phanerozoic, but it becomes even higher with $f_{AW10}$_$f_A$. A steep decline immediately follows this peak, coincident with the Hirnantian icehouse. Conversely, $f_{AW10}$_$f_A$ values during the LPIA and the End Cenozoic Icehouse Age (ECIA) remain comparable to the original values ($f_{AW}$_$f_A$ around 1). The values during the Devonian, which already had the lowest Phanerozoic $f_{AW}$_$f_A$, become even lower. However, if we further adjust $f_{AW10}$_$f_A$ for the effects of equatorial aridity between 270 and 110 Ma (''adjusted $f_{AW10}$_$f_A$''), then the late Permian to mid-Cretaceous greenhouse is characterized by the lowest recorded Phanerozoic $f_{AW10}$_$f_A$ values (around 0.4). In fact, these refinements made to account for aridity in the adjusted $f_{AW10}$_$f_A$ result in a lowering of the values to less than half of that of the present-day for the majority of the Mesozoic (Fig. 9b). Given the large differences exhibited by these alternative estimations of $f_{AW}$_$f_A$, the specific selection of $f_{AW10}$_$f_A$ unsurprisingly has a profound influence on $CO_2$ modelling (Section 5).

### 4.2. Revised degassing ($f_{SR}$)

For $CO_2$ modelling (Section 5) we have defined $f_{SR}$ in two different ways. In the first case, we use a hybrid version where $f_{SR}$ is estimated from the subduction flux back to 350 Ma and then we switch to using the normalized zircon age distribution (hereafter 'arc-activity') as a measure of $f_{SR}$ for all earlier times. In the second case, we simply use arc-activity as a measure of $f_{SR}$ for the entire time range (Fig. 8a; Supplementary data 2, Table S1). Continental arc-activity has been argued to play an important role in regulating long-term climate changes, and McKenzie et al. (2016) argued that reduced continental arc activity explains all icehouse climates. Only the LPIA, however, shows a clear relation with the zircon record, and the ECIA occurred long after the onset of a large reduction in arc activity which started in the Cretaceous. In our analysis, there is a general decrease in arc activity during the Ordovician but the short-lived end-Ordovician (Hirnantian) icehouse was not preceded by any notable changes in the arc activity curve, which continued descending until reaching a minimum during the Devonian (Fig. 8a). That was at a time when the climate was generally warm, although there are rocks of glacial origin in the latest Devonian and earliest Carboniferous of South America (Torsvik and Cocks, 2017). Another minimum in arc activity that coincided with prevailing greenhouse conditions occurred during the Triassic-Early Jurassic. Thus, variations in plate tectonic activity/degassing cannot alone explain greenhouse versus icehouse conditions.

Over the past few years, $f_{SR}$ has been estimated in many ways, and in Fig. 8b we compare our estimate of $f_{SR}$, using normalized arc activity (as in Fig. 8a) as a proxy, with two other estimates that are available for the entire Phanerozoic (and older times): the standard $f_{SR}$ in GEOCARBSULF (Berner, 2004) and a hybrid $f_{SR}$ estimate based on subduction and rift lengths (Mills et al., 2019). Our estimates of $f_{SR}$ (based on arc activity) show a minimum during the late Neoproterozoic (Cryogenian) Snowball Earth events (not shown in the diagram), followed by a steady increase in the late Precambrian-early Cambrian, and peak at 520 Ma (P#1 in Fig. 8). A corresponding $f_{SR}$ value of about 1.8 is similar to the two other estimates but the $f_{SR}$ curves are very different for most of the Paleozoic. The Hirnantian Icehouse (probably lasting less than a million years) is not recognized in any of the curves for $f_{SR}$ (Fig. 8b) and our $f_{SR}$ values vary between 1.5 and 1.4 during the Ordovician. Our arc activity peak in the early Carboniferous (P#2, Fig. 8b) is not recognized in the two other curves but a general low during the LPIA is seen in all curves. During the Mesozoic, the hybrid curve of Mills et al. (2019) is close to our curve, whilst the Berner (2004) seafloor production curve is much lower. All curves peak in the Early Cretaceous with $f_{SR}$ values of 2.4–1.5, followed by decreasing values toward recent times. Our arc activity peaks P#3 and P#4 are not reflected in the two other curves, but on average the trend of the $f_{SR}$ curve of Mills et al. (2019) follows our arc activity curve (Fig. 8b). Note, however, that we have shown subduction lengths from full-plate models to be an over-simplified measure of $f_{SR}$ (Section 3.3) and thus the hybrid $f_{SR}$ estimate of Mills et al. (2019) may be less reliable prior to 200 Ma.

Merdith et al. (2021) recently published a full-plate model for the past one billion years, from which we can extract a subduction flux. Some similarities to our subduction flux in the late Paleozoic could be anticipated given that this model is based on the model of Young et al. (2019), which in turn modified the model of Domeier and Torsvik (2014). Young et al. (2019) made substantial changes to the model of Domeier and Torsvik (2014), but several of these involved latitudinal adjustments that violated paleomagnetic constraints and were subsequently reverted by Merdith et al. (2021), so the latter model more closely resembles that of Domeier and Torsvik (2014). However, significant differences remain in the assignment of longitudes between these models (see below). For 500–410 Ma, the Merdith model is adapted from two regional models (Domeier, 2016, 2018) and in earlier time it connects with the Neoproterozoic model of Merdith et al. (2019).

Differences in the late Paleozoic subduction flux (Fig. 8b) between Merdith et al. (2021) and this study, most notably a peak at 320 Ma (start of LPIA), result largely from longitudinal changes made with respect to the model of Domeier and Torsvik (2014). The observation of a large difference at 320 Ma might initially appear counterintuitive since Pangea is assembled by this time in both models, and positioned at similar longitudes (although note Merdith et al. (2021) reconstruct Pangea farther north than what the bulk of paleomagnetic data suggest at this time). Recalling that the subduction fluxes shown in Figs. 6 and 8 are scaled (relative to

**Table 2**
Overview of the 12 different models we have used to estimate atmospheric $CO_2$ in the GEOCARBSULFvolc program. All parameters as in Royer et al. (2014) except time-dependent changes in $f_{SR}$, $f_A$ and $f_{AW\_A}$. In the original GEOCARBSULF code these parameters are described as *"Seafloor creation rate at time (t) relative to the present-day"* ($f_{SR}$), *"Land area at time (t) relative to the present-day"* ($f_A$) and *"Fraction of land area undergoing chemical weathering"* ($f_{AW\_A}$ & $f_{AW10\_A}$). For the latter two parameters we use those of Royer et al. (2014) before 520 Ma.

| Model | Revised parameter descriptions (others as in Royer et al. 2014) |
|---|---|
| M1 | Revised $f_A$ and $f_{AW\_A}$ scaled by exposed land within ±10° and between 40 and 50°N/S (Fig. 11a, 9) |
| M2 | As M1 but $f_{AW\_A}$ adjusted for arid equatorial regions (Fig. 11a, 9) |
| M3 | Revised $f_{SR}$ (arc-zircon model) (Fig. 11b, 8a) |
| M4 | Revised $f_{SR}$ (hybrid model: Subduction flux 0–350 Ma and arc-zircon model for older times) (Fig. 11b, 8a) |
| M5 | M2 + M3 (Fig. 11c, 13a) |
| M6 | M2 + M4 (Fig. 11c) |
| M7 | Revised $f_A$ and $f_{AW10\_A}$ (Fig. 12a, 9) |
| M8 | M7 + M3 (Fig. 12a, 9) |
| M9 | M7 + M4 (Fig. 12b, 9) |
| M10 | As M7 but $f_{AW10\_A}$ adjusted for arid equatorial regions (Fig. 12b, 9) |
| M11 | As M8 but $f_{AW10\_A}$ adjusted for arid equatorial regions (Fig. 12b, 9) |
| M12 | As M9 but $f_{AW10\_A}$ adjusted for arid equatorial regions (Fig. 12b, 9, Fig. 13a) |

present-day rates), this difference arises because the model of Domeier and Torsvik (2014) includes stronger longitudinal motions prior to Pangea formation necessitated by the absolute reference frame (Torsvik et al., 2014). By contrast, the models of Merdith et al. (2021) and Young et al. (2019) are not longitudinally anchored, and therefore have generally smaller rates of tectonic motion for all times prior to Pangea formation.

In early Paleozoic time, the subduction flux from Merdith et al. (2021) shows large fluctuations in the late Cambrian and Early Ordovician, and very low (as today) rates in the earlier Cambrian. Interestingly, an accelerated subduction flux (increased $CO_2$ sourcing) occurs during the Hirnantian glaciation, although this signal is not recognized in any other models (Fig. 8b). Importantly, this subduction flux does not resemble the normalized arc-related zircon age distribution prior to 400 Ma. Although improving plate models certainly hold the promise of providing stronger constraints on solid Earth degassing in such deep time, there remain substantial uncertainties and ambiguities in global paleogeography in Ediacaran and earliest Paleozoic time (e.g. Abrajevitch and Van der Voo, 2010), which have a direct impact on reconstructions extending into the early Paleozoic. We therefore consider the normalized arc-related zircon age distribution to be a presently better proxy for arc-activity and potential carbon degassing in deep time.

## 5. $CO_2$ modelling

The most recent GEOCARBSULFvolc model (described in Royer et al., 2014) can be run with two different sets of paleogeographic parameters (that we here revised) but also runoff ($f_D$) and temperature (GEOG) input parameters ('*Berner*' or '*Goddéris*' in Royer et al., 2014). We used the *Goddéris* weathering parameters ($f_D$ and GEOG, Fig. 1 in Royer et al., 2014) with our modifications of $f_A$, $f_{AW}f_A$, and $f_{SR}$ to generate new $CO_2$ estimates presented here. The code and resampling strategy were applied as in Royer et al. (2014): the model was run with 10,000 iterations for each of our tests. Following the strategy of Royer et al. (2014), each revised parameter was tested separately with decreasing error percentage applied, from 50 to 30% on average, until the model failure rate reached levels below 5%. The presented simulations estimate atmospheric $CO_2$ for the past 570 Myrs in 10 Myr intervals and assume a steady state between those time steps (Berner, 2004). Only simulations between 520 Ma and present-day are shown here to coincide with the resolution of our paleogeographic reconstructions and therefore our revised paleogeographic input.

We tested many different scenarios to assess the relative influence of the revised input parameters (Table 2). We first tested separately the influence of paleogeography by changing only the paleogeographic inputs, as well as considering revised climate gradients for parts of the late Paleozoic and Mesozoic. We then tested the influence of two different proxies for degassing (i.e. subduction flux vs. arc activity). Finally, we tested different combinations of changes in paleogeography and degassing. Revised simulations (Models 1–12) are shown in Figs. 11 and 12 and reconstructed $CO_2$ levels are plotted together with proxies extending back to the Early Devonian (Foster et al., 2017) as well as the GEOCARBSULFvolc simulation of Royer et al. (2014) for comparison.

### 5.1. Phanerozoic $CO_2$ fluctuations from GEOCARBSULFvolc model simulations (Royer et al., 2014)

The Royer et al. (2014) model predicts very high $CO_2$ levels in the early Cambrian (520 Ma), close to 5000 ppm on average, which peak at 6000 ppm at 540 Ma (see supplementary data 2, Table S2). Those values drop rapidly throughout the late Cambrian and Early to mid-Ordovician to about 2000 ppm, followed by a further drop in the Late Ordovician-early Silurian to about 1800 ppm. The early Paleozoic, therefore, witnessed a reduction in $CO_2$ levels of about 4000 ppm (Fig. 11, blue curve). During the late Silurian-Early Devonian, there is an increase in $CO_2$ levels to about 2400 ppm before a major decline to about 350 ppm by the early Carboniferous (350 Ma). This major shift in Earth history is contemporaneous with the origin and expansion of Devonian forests (Berner, 1997), and the reduction in modelled $CO_2$ (Fig. 11, blue curve) closely follows that of the proxies (red stippled curve with yellow confidence envelope).

$CO_2$ levels average 357 ppm between the early Carboniferous (350 Ma) and the late Permian (260 Ma). Those low values (extending throughout the LPIA) are comparable to 'modern-day' $CO_2$ levels. Near the Permo-Triassic boundary, there is a sharp increase in modelled $CO_2$ levels from about 380 ppm at 260 Ma to about 1250 ppm at 250 Ma. This increase is due to the combined effect of low land-availability for silicate weathering and low runoff triggering a low weathering activity, but also to the low values in the isotopic time series of $\delta^{13}C$ and $\delta^{34}S$ used to track carbon burial through time (Fig. 1b,c,h in Royer et al. 2014). This important reduction of the $CO_2$ sinks with stable degassing (Fig. 1k in Royer et al. 2014) lead to the simulation of this peak. Furthermore, the peak is partly driven by a drop in climate sensitivity from 6 °C per doubling of $CO_2$ during the LPIA (330–260 Ma in the GEOCARBSULFvolc code) to 3 °C from 250 Ma and onwards (until 30 Ma and the start of the end-Cenozoic Ice Age); a lower climate sensitivity leads to larger changes in atmospheric $CO_2$ due to weaker associated silicate weathering feedbacks. This change in climate sensitivity implemented in GEOCARBSULFvolc is based on geological evidence of a long-term climate sensitivity of 6 °C or higher during

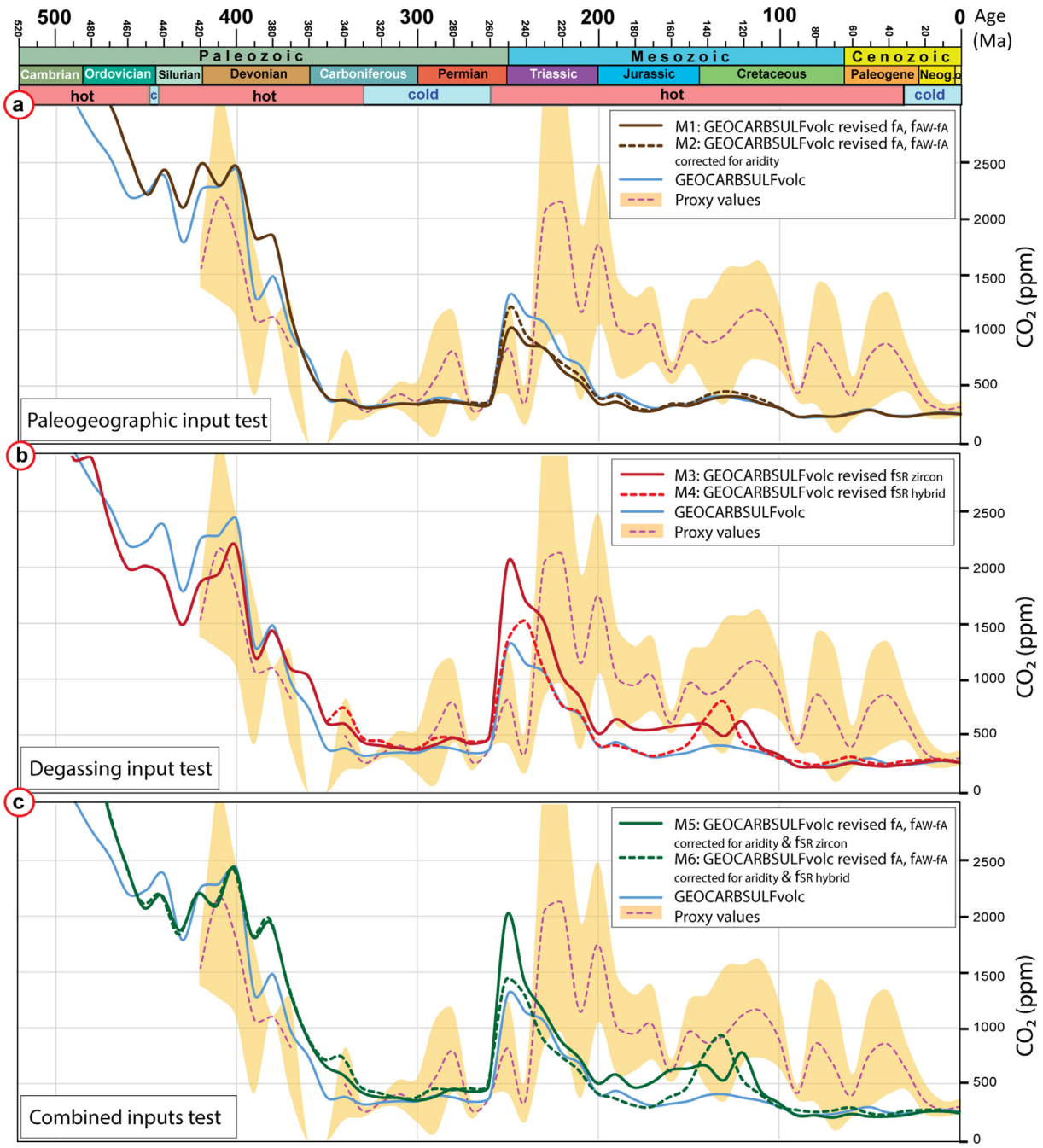


**Fig. 11.** Timescale with greenhouse (hot) versus icehouse (cold) conditions for the past 520 Myrs (see Fig. 3 caption) and modelled $CO_2$ levels with GEOCARBSULFvolc (a) Simulations with revised input for paleogeography (full line) and reduced exposed land due to arid climate during Pangea (dotted line) (b) Simulations with revised degassing input parameter with arc zircons as a proxy (full line) and subduction flux (dotted line). (c) Simulations with both revised parameters from a) and b). The yellow shaded area corresponds to $CO_2$ proxy values from Foster et al. (2017). The purple dashed line shows the median value of the proxies. Simulated $CO_2$ levels for the Cambrian-Early Ordovician exit the scale of display (levels reaching above 6000 ppm) but can be found in Table S2 in the supplementary data 2. The blue curve in a) b) and c) is the simulation for the Phanerozoic using GEOCARBSULFvolc as in Royer et al. (2014).

those icehouses (Hansen et al., 2008; Pagani et al., 2010; Park and Royer, 2011; Rohling et al., 2012; in Royer et al., 2014). Subsequently, a drop in modelled $CO_2$ levels follows the 250 Ma peak and $CO_2$ levels in the Royer et al. (2014) model remain below 500 ppm from the Early Jurassic onward.

### 5.2. Revised models

When considering only the revised paleogeographic (weathering related) input parameters, i.e. $f_A$ and with total weatherability taken to be $f_{AW}f_A$ (brown line in Fig. 11a, Model M1), we observe two notable changes in the modelled $CO_2$ levels compared to the previous GEOCARBSULFvolc model (blue curve, Fig. 11a). First, modelled $CO_2$ levels in the early Paleozoic (Caldeira, 1992; Hansen et al., 2008; Pagani et al., 2010; Rohling, 2012) are on average 300 ppm higher until the Late Devonian. Second, the Permo-Triassic peak at 250 Ma is reduced by 500 ppm. The revised quantification of exposed land being weathered at low latitudes in 'Central Pangea' from 270 Ma due to aridity (Fig. 9b, red stippled curve), only result in marginally higher $CO_2$ levels during the late

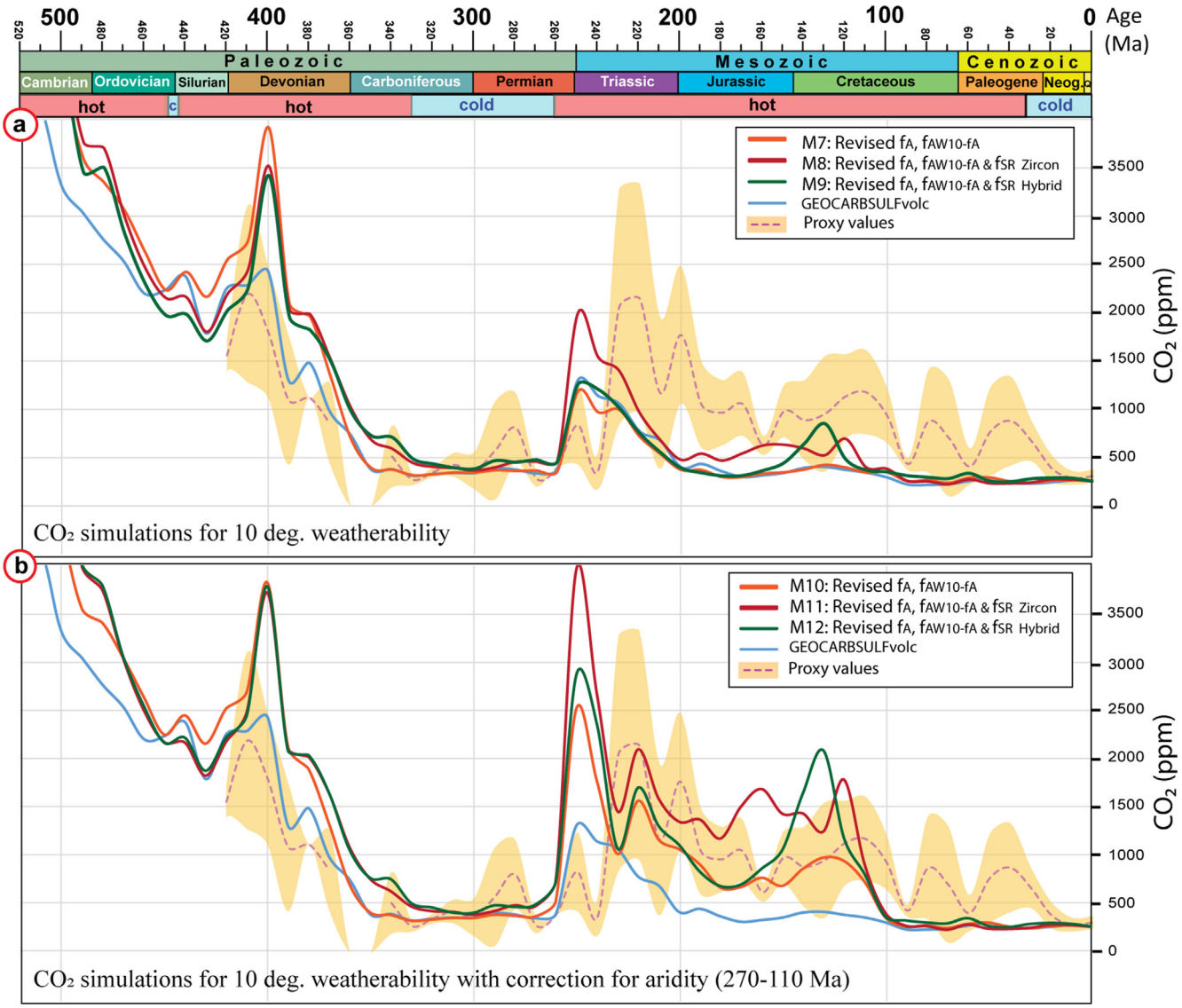


**Fig. 12.** Timescale with greenhouse (hot) versus icehouse (cold) conditions for the past 520 Myrs (see Fig. 3 caption) and (a) simulations with revised paleogeographic input for only the ±10° latitudes as weatherability (orange curve), together with new degassing input using zircon as a proxy (red curve) or hybrid subduction flux/zircon as a proxy (green curve). The yellow shaded area corresponds to $CO_2$ proxy values from Foster et al. (2017). The purple dashed line shows the median value of the proxies. Simulated $CO_2$ levels for the Cambrian-Early Ordovician exit the scale of display (levels reaching above 6000 ppm) but can be found in Table S3 in the supplementary data 2. (b) Similar simulations as in panel (a) but with additional refinements in paleogeographic input due to arid tropical areas between 270 and 110 Ma. The blue curve in both a) and b) is the simulation for the Phanerozoic using GEOCARBSULFvolc as in Royer et al. (2014). Simulated $CO_2$ levels for the Cambrian-Early Ordovician exit the scale of display (levels reaching above 6000 ppm) but can be found in Table S3 in the supplementary data 2.

Paleozoic and Mesozoic. Indeed, $CO_2$ levels are only 50 ppm higher on average after 250 Ma, even though these revisions reduce the weathering sink quite considerably (Fig. 11a, Model M2).

The revision of the degassing parameter ($f_{SR}$) leads to a different response compared with the reference model of Royer et al. (2014) (blue curve in Fig. 11b). Our revised model(s) show lower $CO_2$ levels during the early Paleozoic (except for the Cambrian) and higher levels during the late Paleozoic and Mesozoic until the mid-Cretaceous (Fig. 11b, red curves). We modelled $CO_2$ with two different estimates of $f_{SR}$: In the first case, we used subduction flux as a proxy back to 350 Ma and then continued backward in time with the use of arc activity as a proxy for $f_{SR}$ (hybrid version; stippled red curve in Fig. 11b, Model M4). In the second case, we only used arc activity for the $f_{SR}$ proxy (thick red curve in Fig. 11b, Model M3). Both cases yield similar $CO_2$ levels for the Paleozoic results, whilst the Permo-Triassic $CO_2$ peak and Mesozoic levels differ more markedly (Fig. 11b). Using arc activity as a proxy for degassing leads to higher $CO_2$ estimates at the Permo-Triassic boundary with values above 2000 ppm, whilst the subduction flux proxy yields levels around 1500 ppm. This drop is probably linked to the switch in the full-plate models used to calculate the subduction flux (Fig. 8a). Globally, the use of arc activity as $f_{SR}$ proxy leads to higher $CO_2$ levels during Triassic to Early Cretaceous times and brings the modelled $CO_2$ estimates closer to the envelope of proxy values for $CO_2$. Subduction flux as a proxy for degassing during the Mesozoic (Model M4) leads to a single pronounced $CO_2$ peak at 130 Ma compared with the standard model (Fig. 11b).

When used simultaneously, the use of our revised input parameters (i.e. $f_{AW}$ $f_A$ and $f_{SR}$ together) leads to higher $CO_2$ levels in the Cambrian and Early Ordovician (570–450 Ma) with levels on average 1500 ppm higher than the previous model (Fig. 11c and Supplementary data 2, Table S2 for the early Cambrian). During the mid-Ordovician to Devonian, the levels are similar to the previous GEOCARBSULFvolc model (Fig. 11c). From the mid-Devonian, the

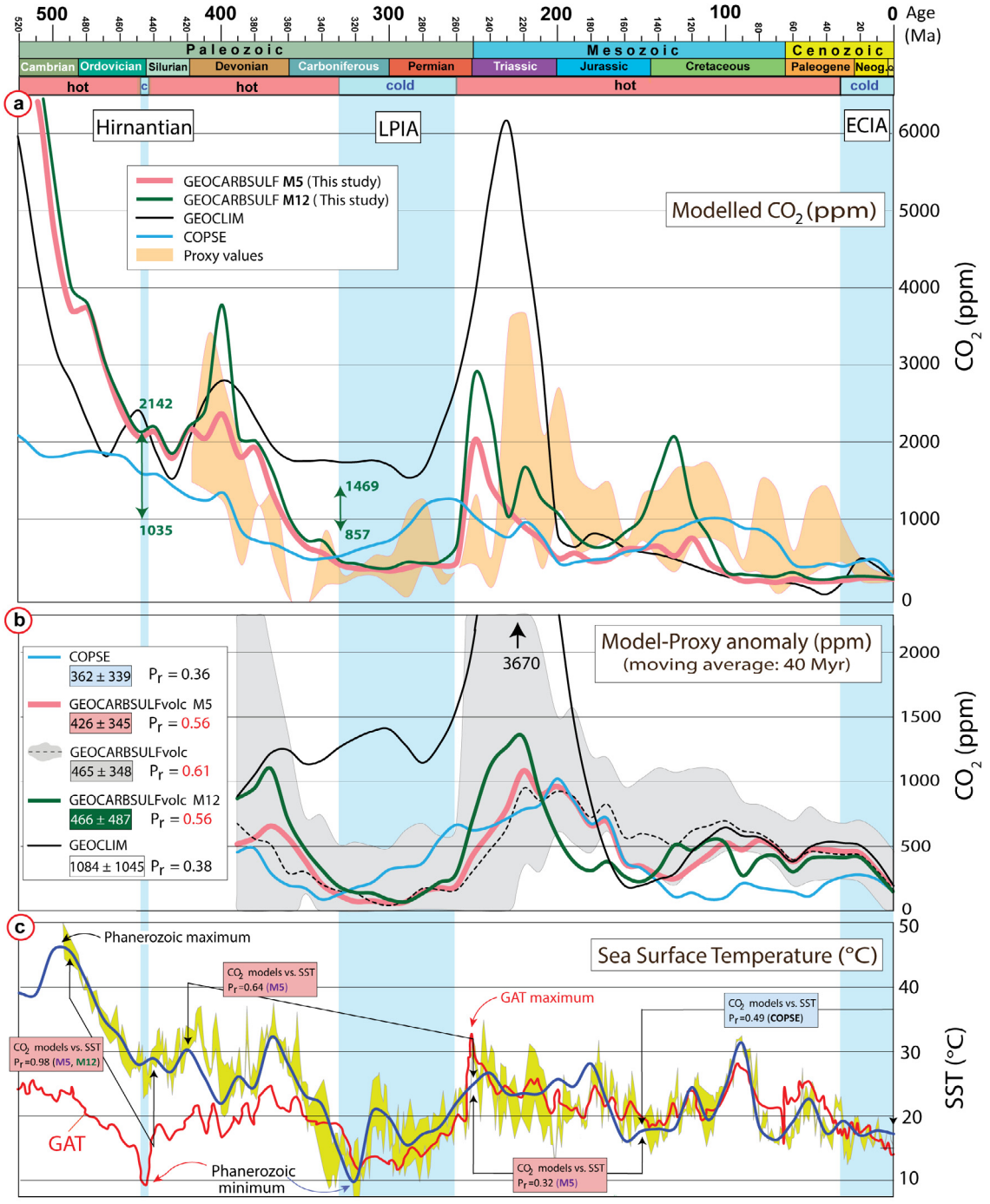


**Fig. 13.** Timescale with greenhouse (hot) versus icehouse (cold) conditions for the past 520 Myrs (see Fig. 3 caption) and (a) $CO_2$ simulations with GEOCARBSULFvolc using revised paleogeography weathering parameters (with correction for aridity) and arc activity (zircons) as a proxy for degassing (Model M5: red thick curve; Tables S2-S3 of the supplementary data 2), and with weatherability only at ±10° and hybrid proxy for degassing (Model M12: green curve). GEOCLIM (GEOCLIMTec in Goddéris and Donnadieu, 2017; Goddéris et al., 2014), and COPSE (Mills et al., 2019) are also plotted against $CO_2$ proxy values from Foster et al. (2017) with 95% standard deviation confidence envelopes for each 10 Myrs interval. The green arrows with numbers at the onset of the Hirnantian and Late Paleozoic Ice Age are estimated $CO_2$ thresholds to initiate continental-scale glaciations with a fainter sun back in time and assuming a modern threshold of 500 ppm for recent times (Royer, 2006), and considering temperature changes due to luminosity only. High (low) numbers assume a climate sensitivity of 3 °C (6 °C) per doubling of $CO_2$. Simulated $CO_2$ levels for the Cambrian-Early Ordovician exit the scale of the diagram (levels reaching above 6000 ppm) but can be found in Tables S2 and S3 of the supplementary data 2. (b) Model-Proxy anomalies for all the models in panel a plus GEOCARBSULFvolc (Royer et al., 2014) shown with 95% confidence envelopes. Anomalies have been smoothed with a moving window (40 Myrs) and thus start at 400 Ma. (c) Sea surface temperatures (SSTs) shown as 95% confidence envelope in yellow shading (Song et al., 2019) and a filtered running mean (5 Myr window) SST curve (blue line) extended back to 520 Ma (see Section 6 for details). The red line is the temperature (GAT) curve of Scotese et al. (2021), extensively based on the SSTs of Song et al. (2019), but modified (most notably for the Paleozoic) by adding or subtracting temperatures from the SSTs based on geological and paleontological criteria according to the authors. The labels refer to the Pearson coefficient analysis ran between the two curves mentioned in the label and over the interval shown between the arrows linked to the label.

use of our revised parameters leads to higher modelled $CO_2$ levels, and the response is even higher for the small peak simulated at 380 Ma where levels go up by 500 ppm (Fig. 11c). This increase in $CO_2$ can clearly be attributed to the change in paleogeographic input as simulations remain similar to the previous GEOCARBSULFvolc model (blue curve) when testing the effect of degassing in M3 or M4 (Fig. 11 b). However, higher estimates in the Mesozoic clearly relate to the choice of degassing input. Even associated with the revised paleogeographic input, the use of arc activity as a proxy for degassing leads to a higher estimated peak in $CO_2$ at 250 Ma, and generally higher $CO_2$ levels throughout the Jurassic and Early Cretaceous (solid green line in Fig. 11c, Model M5).

To assess the impact of the definition of weatherability, we also ran simulations wherein weatherability was restricted to the equator where silicate weathering potential is at its maximum (if physical erosion allows it). With this definition, we recalculated $f_{AW}f_A$ by only considering exposed land near the equator (±10°, e.g. using $f_{AW10}f_A$) and tested its influence with and without refinement linked to aridity that developed across central Pangea, as well as combined with our revised degassing estimates. This change from $f_{AW}f_A$ to $f_{AW10}f_A$ does not drastically change the $CO_2$ estimates, even when associated with our degassing revisions, but intensifies the $CO_2$ peak at 400 Ma (Fig. 12a, orange curve, Model M7) and results in a minor elevation of modelled $CO_2$ levels during Triassic-Jurassic time. However, when refined for aridity in the equatorial belt (Models M10-12), changes in $f_{AW10}f_A$ make the models highly responsive and sensitive to changes in degassing (Fig. 12b).

Indeed, the reduction of exposed land available to weathering during Pangea times is translated into a sharp rise in $CO_2$ levels (orange curve in Fig. 12b) and the additional effect of elevated degassing leads to much higher $CO_2$ estimates for most of the Mesozoic (Fig. 12b). The increased $CO_2$ levels lead overall to a better apparent fit with the proxy values, even if the peaks simulated are higher than the proxy values between 160 and 120 Ma (Fig. 12b). A particularly good fit is observed between the estimates and the proxy values between 230 and the peak at 220 Ma, which is triggered by a rebound in land availability and is notably absent in the previous GEOCARBSULFvolc model of Royer et al. (2014) (Figs. 12b & 9b).

## 6. Discussion

In Fig. 13 we compare two of our GEOCARBSULFvolc models (M5 and M12; see supplementary data 2, Tables S2 and S3 for times before 520 Ma) with (*i*) two other long-term carbon cycle models (GEOCLIM and COPSE), (*ii*) proxies for $CO_2$ (when available), and *(iii)* sea surface temperatures (SSTs). SSTs are plotted in 10 Myrs intervals and each mean temperature is calculated over a five Myr window (blue thick curve in Fig. 13c). We use the dataset of Song et al. (2019), assuming an invariant oxygen isotope composition of seawater to calculate SSTs, and data-selection includes only $\delta^{18}O$ from phosphate fossils (apatite conodonts) before the Mesozoic. We have extended the dataset of Song et al. (2019) to ~520 Ma with $\delta^{18}O$ data from phosphatic Siberian brachiopods (Wotte et al. 2019). To assure that we only included fossils that once thrived in (shallow) seas at low latitudes, we excluded reconstructed fossil locations above ±30°. Because of this and the fact that our SST curve is smoothed our mean values may at times not overlap with the 95% confidence envelope of Song et al. (2019). The mean reconstructed latitude is 16 ± 9° for the past 520 Myrs (based on own reconstruction parameters) and mean latitudes are similar for Paleozoic (14 ± 8°) and Mesozoic/Cenozoic times (17 ± 9°).

**Table 3**
Pearson correlation coefficients for different time-series. (a) Testing correlation between models and $CO_2$ proxies for different time periods. (b) Testing correlation between models. (c) Testing correlation between models and sea surface temperature for different time periods. All the revised paleogeographic inputs include corrections for aridity (Models M5 and M12; see Table 1 and Fig. 13a). In Table 3a we have also averaged model-proxy differences over selected time periods (see also Fig. 13c). [#1]Royer et al. (2014); [#2]Goddéris and Donnadieu (2017); [#3]Mills et al. (2019).

(a) Pearson C - models versus $CO_2$ proxies (Coverage 420–0 Ma)

| Time period (Ma) | M5 (this study) | M12 (this study) | GEOCARBSULFvolc[#1] | GEOCLIM[#2] | COPSE[#3] |
|---|---|---|---|---|---|
| Late Paleozoic (420–250) | 0.87 | 0.83 | 0.94 | 0.41 | 0.53 |
| Paleozoic selection (420–270) | 0.91 | 0.89 | 0.95 | 0.76 | 0.62 |
| Mesozoic/Cenozoic (230–0) | 0.78 | 0.61 | 0.79 | 0.76 | 0.40 |
| Cenozoic (70–0) | −0.95 | −0.43 | −0.29 | −0.29 | 0.11 |
| Phanerozoic (420–0) | 0.56 | 0.57 | 0.61 | 0.38 | 0.36 |
| **Mean Model-Proxy offsets (in ppm) and standard deviation (1σ)** | | | | | |
| Phanerozoic (420–0) | 426 ± 345 | 467 ± 487 | 465 ± 348 | 1084 ± 1045 | 363 ± 339* |
| Paleozoic selection (420–270) | 290 ± 271 | 428 ± 482 | 305 ± 308 | 1174 ± 374 | 351 ± 270 |
| Mesozoic/Cenozoic selection (230–0) | 476 ± 332 | 382 ± 307# | 554 ± 325 | 726 ± 932 | 349 ± 386* |

(b) Pearson C – Our new models against other models

| | M5 vs GEOCARSULFvolc | M12 vs GEOCARBSULFvolc | M5 vs GEOCLIM | M5 vs COPSE |
|---|---|---|---|---|
| Early Paleozoic (540–420) | 0.92 | 0.92 | 0.86 | 0.82 |
| Late Paleozoic (420–250) | 0.96 | 0.93 | 0.65 | 0.41 |
| Early Mesozoic (250–150) | 0.93 | 0.85 | 0.71 | 0.84 |
| Late Mesozoic (150–70) | 0.86 | 0.90 | 0.88 | −0.02 |
| Cenozoic (70–0) | 0.17 | −0.17 | 0.89 | 0.17 |
| PHANEROZOIC (520–0) | 0.98 | 0.96 | 0.67 | 0.86 |

(c) Pearson C- models versus sea surface temperature (SST, coverage 520–0 Ma)

| | M5 | M12 | GEOCARBSULFvolc | GEOCLIM | COPSE | Proxies vs SST |
|---|---|---|---|---|---|---|
| Early Paleozoic (520–420) | 0.70 | 0.70 | 0.61 | 0.50 | 0.72 | |
| 'Ordovician' (490–440) | 0.97 | 0.99 | 0.93 | 0.66 | 0.83 | |
| Late Paleozoic (420–250) | 0.65 | 0.55 | 0.56 | 0.34 | 0.12 | 0.53 (0.94 for 370–320 Ma) |
| Early Mesozoic (250–150) | 0.32 | 0.27 | 0.44 | 0.31 | 0.10 | 0.12 |
| Late Mesozoic (150–70) | −0.17 | −0.33 | −0.26 | −0.32 | 0.49 | −0.42 |
| Cenozoic (70–0) | −0.17 | 0.00 | 0.52 | −0.35 | −0.36 | 0.27 |
| PHANEROZOIC (520–0) | 0.82 | 0.77 | 0.81 | 0.44 | 0.73 | 0.40 (420–0 Ma) |

Models M5 and M12 are especially highlighted because they yield the lowest model-proxy residuals, notably for the Mesozoic (Fig. 12 and Table 3a). Model M5 also has low residuals (mean = 290 ± 271 ppm) during the late Paleozoic (420–270 Ma). Conversely, M12 has comparatively low residuals over the last 230 Myrs (382 ± 307 ppm; Table 3a). As a reminder, model M5 incorporates changes in both paleogeographic/weathering ($f_A$ and $f_{AW}$–$f_A$ scaled by exposed land within the warm/wet tropics and the northern/southern wet-belts, and corrected for arid equatorial regions) and degassing ($f_{SR}$) parameters. The latter is based on normalized arc-activity (zircons) and this $f_{SR}$ proxy is available for the entire Phanerozoic. Model M12 differs in two ways: $f_{AW}$–$f_A$ is only scaled by exposed land within the warm/wet tropics ($f_{AW10}$–$f_A$), and as a proxy for $f_{SR}$ we use the hybrid model (Table 3). To quantitatively compare different models against proxy $CO_2$, we compute the residuals for each step as well as the Pearson's correlation coefficients ($P_r$) (Table 3). We also show graphically a 40 Myr moving average of the residuals in Fig. 13b. Over the last 420 Myrs, COPSE has a slightly lower $P_r$ than GEOCLIM (0.36 and 0.38, respectively) (Fig. 13b), whilst the GEOCARBSULFvolc models provide higher values ($P_r$ = 0.56–0.61; Table 3a). However, $CO_2$ models are associated with considerable uncertainties (not shown for our models), and one sigma errors in the GEOCARBSULFvolc model (e.g., Royer et al., 2014) averages to 350 ppm for the past 570 Myrs. Thus, most of the model and proxy $CO_2$ values (Fig. 13a,b) overlap within error at the 95% confidence level.

There are no reliable $CO_2$ proxies before the Early Devonian and therefore the reliability of long-term carbon cycle models is more difficult to evaluate for the early Paleozoic. Although $CO_2$ proxies based on marine organic matter have been presented by Witkowski et al. (2018), we note that there are outstanding questions concerning the fidelity of these proxies under conditions of high $CO_2$, and we therefore disregard them (Witkowski et al., 2019).

All models, including ours, suggest a systematic decrease in $CO_2$ levels of 3000–4000 ppm in the early Paleozoic (Fig. 13a, supplementary data 2, Tables S2-S3). This decrease corresponds to an increase in theoretical weatherability (Fig. 5c, red curve), and notably exposed land within the warm and wet tropics (Fig. 5a, red curve). This drop in $CO_2$ levels coincides with a strong reduction in sea surface temperatures (SSTs) from ~500 Ma (Fig. 13c), reaching a low just prior to the short-lived Hirnantian icehouse at ~445 Ma. In our analysis, this cooling correlates with a peak in land availability to weathering in the Late Ordovician but also to a reduction in arc-activity during the early Paleozoic (Fig. 8). Thus, the combination of enhanced silicate weathering and decreased degassing can explain a global cooling towards the end-Ordovician in our models.

The Hirnantian cooling event has been considered paradoxical due to its apparent association with high $CO_2$ levels (e.g., Vandenbroucke et al., 2010, Crowley and Baum,1995), as observed in all our tested carbon cycle models (1620–2430 ppm, Fig. 13a; Supplementary data 2, Tables S2-S3). Low atmospheric $CO_2$ is a principal variable in controlling continental-scale glaciations, but the solar energy was lower (by 3–5%) in the Late Ordovician (Crowley and Baum, 1995). Consequently, the $CO_2$ threshold for nucleating ice sheets during this period may have been 4–8 times higher than pre-industrial levels of ~280 ppm (Gibbs et al. 2000; Herrmann et al. 2003; Royer, 2006; Lowry et al. 2014). The study of the response of temperature per doubling of atmospheric $CO_2$, i.e climate sensitivity, can help us to estimate the threshold for glaciation initiation. The combined study of $CO_2$ proxies and temperature generally show climate sensitivities of about 3 °C per $CO_2$ doubling during ice-free periods, and about 6 °C per doubling $CO_2$ with land ice (Royer, 2016). Estimated $CO_2$ thresholds to initiate continental-scale glaciations with a fainter sun in the end-Ordovician varies between 1035 and 2142 ppm (Fig. 13a) based on a climate sensitivity of 6 °C and 3 °C per doubling of $CO_2$, respectively. These estimates assume a modern threshold of 500 ppm for recent times (Royer, 2006) and only consider temperature changes due to luminosity differences. All models are within or close to the theoretical threshold values (Fig. 13a). In our GEOCARBSULFvolc simulations, we used a constant climate sensitivity of 3.0 ± 1.25 °C per $CO_2$ doubling, except during glacial periods (LPIA, ECIA) where climate sensitivity doubles to 6 °C as in Royer et al. (2014).

The proxy record shows high levels at 410 Ma followed by a decrease in $CO_2$ levels toward the LPIA (Fig. 13a), whereas all models suggest a peak at 400 Ma. Considering uncertainties in both proxies and models, $CO_2$ levels in our GEOCARBSULFvolc model M5 and COPSE overlap with $CO_2$ proxy levels for the late Paleozoic and with strong to moderate $P_r$'s of 0.87 and 0.53, respectively (420–250 Ma, Table 3a). Our GEOCARBSULFvolc simulations suggest a strong decrease of more than 2500 ppm during the Devonian and early Carboniferous and bring $CO_2$ levels under 500 ppm during the LPIA, as also indicated by the proxies (Fig. 13a, b). The GEOCLIM model shows a more modest drop of 1000 ppm and modelled $CO_2$ levels are above 1500 ppm during the LPIA, twice that of the proxy estimates, and the $P_r$ for the late Paleozoic is poorer ($P_r$ = 0.41, Table 3a) than the other models for the period 420–250 Ma. However, new simulations using GEOCLIM that focus specifically on the late Paleozoic yield lower $CO_2$ levels (down to 400 ppm for some simulations) during the LPIA (Goddéris et al., 2017), more in line with with simulations using GEOCARBSULFvolc, including ours, and the proxy record.

SSTs and modelled $CO_2$ (GEOCARBSULFvolc and GEOCLIM) correlate well for the early Paleozoic (520 to 420 Ma, see also Cocks and Torsvik, 2020) yielding a $P_r$ of 0.6 (0.70 for our revised models M5 & M12) and 0.5, respectively (Table 3a). During the Devonian (400–370 Ma) a marked increase in SSTs (9 °C) occurs 30 Myrs after a prominent increase in $CO_2$ levels. Afterwards, both SSTs and $CO_2$ levels declined progressively towards the initiation of the LPIA in the mid-Carboniferous.

The link between $CO_2$ levels and tropical climate change on million-year timescales has been debated (e.g., Crowley, 1991). The Song et al. (2019) SST curve (yellow confidence envelope in Fig. 13c) included temperature ($\delta^{18}O$) data from fossils that once lived at tropical and subtropical latitudes (<40°N/S). In our reconstructions, a small number of their data points come from paleolatitudes in excess of 40° and so we have restricted the Song et al. (2019) SST curve to only include temperature data from those fossils which lived at latitudes below 30°N/S (Fig. 13c, see supplementary data 3 for SST values). When comparing those selected and smoothed SST data (averaged over 5 Myr bins) to $CO_2$ proxies for different time intervals over the period 420–0 Ma, we observe a similar trend between SST and $CO_2$ proxies ($P_r$ = 0.55, Table 3c) until the late Carboniferous, with a close fit between 370 and 320 Ma ($P_r$ = 0.94). However, for the rest of the Phanerozoic major discrepancies arise between these time series ($P_r$ in Table 3c). Some of these discrepancies could be related to underlying inconsistencies in the data, associated with parameters such as seawater pH, age and the spatial distribution of the SST and $CO_2$ proxies. In addition, the presence of continental ice caps and diagenetic alteration can also affect the accuracy of oxygen isotope paleothermometry (e.g., Song et al., 2019; Scotese et al., 2021; Goldberg et al., 2021). The SST curve also assumes that the sampled organisms lived at shallow water depths and we have assumed an invariant oxygen isotope composition of seawater.

There are also other types of temperature curves such as global average temperatures (GATs), which are an area-scaled integration of all the climate belts. The most recent GAT curve of Scotese et al. (2021) combines geological constraints (e.g., biome maps) and iso-

topic temperature data. This curve shows many similarities to SSTs (Fig. 13c), but its pre-Carboniferous estimates differ radically from high early Paleozoic SSTs, which they reject (but see Goldberg et al. 2021). As a consequence, the GAT curve of Scotese et al. (2021) exhibits minimum temperatures during the Hirnantian Icehouse and maximum temperatures near the Permo-Triassic boundary (Siberian Traps temperature anomaly).

During the mid-late Carboniferous and Permian, GEOCARBSULFvolc models and COPSE simulate low and stable $CO_2$ levels, which are well below the $CO_2$ threshold for nucleating ice sheets during the LPIA (1020–2100 ppm; Fig. 13a). GEOCLIM yields substantially higher $CO_2$ levels during the LPIA followed by a sharp $CO_2$ increase at the end of the LPIA. GEOCARBSULFvolc model M5 yields a noticeable $CO_2$ spike of 2000 ppm at 250 Ma linked to the reduction of $CO_2$ sinks and change in climate sensitivity at this time. This peak is also sensitive to the choice of degassing (see Fig. 11b, c) and is most pronounced when using arc-activity (zircons) as a proxy for $f_{SR}$. The GEOCARBSULFvolc model peak is 20 and 30 Myrs older than the peak in the GEOCLIM model and the proxy peak, respectively. This particular feature but also the difference in intensity of the peak between GEOCARBSULFvolc and GEOCLIM are discussed in Goddéris et al. (2014) and are attributed to the expression of silicate weathering in the models, and how it relates to runoff. Theoretical weatherability is rather constant during the Permian and early Mesozoic (Fig. 9b, red curve) or lowered from about 270 Ma if we consider an arid equator across central Pangea. However, even with variations in the $f_{AW}$_$f_A$ parameter, the GEOCARBSULFvolc model is not very sensitive at the Permo-Triassic boundary (Fig. 11a) and it is the increase in degassing ($f_{SR}$, Fig. 8a) that controls the increased $CO_2$ levels in the model.

Whilst there are first-order, long-term correlations between modelled $CO_2$ levels (GEOCARBSULFvolc and to some extent GEOCLIM), SSTs, $CO_2$ proxies, and the geologic record (continental glaciations) during parts of the Paleozoic (see Pearson correlations in Table 3c), the transition from the LPIA to super-greenhouse conditions at the dawn of the Mesozoic is intriguing. The three carbon cycle models predict very different $CO_2$ levels during this transition; at 230 Ma, for example, modelled $CO_2$ levels vary by more than 5000 ppm. Furthermore, while COPSE shows a peak in the middle Permian, GEOCARBSULFvolc shows a peak (250 Ma) near the Permo-Triassic boundary and GEOCLIM peaks in the mid-Triassic. Note, however, that the elevated $CO_2$ levels in the GEOCARBSULFvolc models (250 Ma) coincide with a reduction in imposed climate sensitivity (from 6 °C to 3 °C), and the large changes in $f_{AW}$_$f_A$ (M10-12; Fig. 9c), which we impose from 280 Ma, have a relatively negligible effect on modelled $CO_2$ (Fig. 13a; green line 280–260 Ma) at high climate sensitivity.

From the Jurassic until the Late Cretaceous, $CO_2$ proxy levels remain relatively stable around 1000 ppm, whereas model values for GEOCARBSULFvolc and GEOCLIM are closer to 500 ppm. COPSE, on the other hand, shows an increase in $CO_2$ from 500 ppm in the Jurassic to 1000 ppm during the mid-Cretaceous (Fig. 13a) and is more compatible with proxy data (Fig. 13b). Our GEOCARBSULFvolc M12 but particularly M5 simulations with revised degassing yield higher $CO_2$ estimates and better match the Mesozoic proxies compared with Royer et al., (2014). However, $P_r$ for both models are poor (Table 3c) and modelled $CO_2$ levels are consistently lower than the proxy values (as with the GEOCLIM model, Fig. 13a).

When including all our revised parameters ($f_A$, $f_{AW}$_$f_A$, and $f_{SR}$), one notable difference from the Royer et al. (2014) model is the elevated $CO_2$ levels in the Early Cretaceous, which visually appear to better fit the proxies, but $P_r$'s remain quite similar for all the GEOCARBSULFvolc models (Table 3a). We have, for some reconstruction times, made rather dramatic changes to estimates of the area of exposed land, but surprisingly, GEOCARBSULFvolc is not very sensitive to these changes, except in the early to mid Paleozoic (until the Late Devonian; Fig. 13a) and at the Permo-Triassic boundary. GEOCARBSULFvolc is more sensitive to our degassing rate ($f_{SR}$) modifications, notably during the Ordovician-Silurian, Carboniferous, Early Triassic and Early Cretaceous.

The testing of a more reduced weatherability ($f_{AW10}$_$f_A$) with refinement for aridity (Fig. 12b) highlights the lack of sensitivity of the model to changes in paleogeography. Indeed, strong differences between the models arise only when the $f_{AW}$_$f_A$ is changed by a factor $\geq$2, as for the peak at 400 Ma between M (1–2, 5–6) and M (7–12) and for the Mesozoic between M (7–9) and M (10–12) with the refinements for aridity (Figs. 11 and 12). Park and Royer (2011) observed this need for a strong reduction in land-availability to achieve a better fit in the model/proxy levels but discarded this option. However, we show here that with refinement due to climate gradients, such a reduction may be reasonable.

With respect to the past 230 Ma, the GEOCARBSULFvolc model with our $f_{AW}$_$f_A$ and $f_{SR}$ (hybrid model) revisions yields the lowest model-proxy difference (382 ± 307 ppm; Table 3a, M12). $P_r$'s, however, remain quite similar between the GEOCARBSULFvolc models. Models using land within ± 10° as a measure of land-area undergoing chemical weathering (e.g. M10 to 12 in Figs. 12b, 13a) are the first simulations that show high $CO_2$ levels in the early Mesozoic and a peak at 220 Ma that better fit the proxy values. However, some important discrepancies remain with the proxy records. Most notably, our refinements for aridity for the models M10-12 lead to very high $CO_2$ being simulated at the Permo-Triassic boundary due to a strong response of the models to the reduced paleogeographic input associated with the already existing low $CO_2$ sinks (i.e., carbon burial and runoff, see Section 5.1) and high climate sensitivity.

The Jurassic is commonly portrayed as a greenhouse world, but episodes of cooler climates have been argued from SSTs (notice the reduction in our smoothed SST curve from about 180 Ma in Fig. 13c; blue thick curve), notably during the Middle and Late Triassic (Dera et al., 2011). Model M12 shows an early Mesozoic low of about 670 ppm in the Middle Jurassic, and proxy data also show a low towards the end of the Jurassic, followed by increasing $CO_2$ levels during the Early Cretaceous. A major discrepancy remains during the late Mesozoic and the Cenozoic between the $CO_2$ proxies (averaging to 500 ppm) and lower simulated levels of $CO_2$ from all of our models (averaging to 250 ppm) (Figs. 11 and 12). The proxy record shows two peaks at 80 and 40 Ma with a mean average value of 800 ppm, whereas our models remain stable at 250 ppm. This discrepancy, notably in the Eocene, was investigated by Park and Royer (2011), who observed an improvement with an enhanced climate sensitivity and a reduction in land availability. On the contrary, our estimations suggest a sharp increase of exposed land during the same time period, leading to greater $CO_2$ consumption (with the caveat that a change of model occurs at 70 Ma) (Fig. 9). In conjunction with that increased $CO_2$ consumption, we also implement a sharp decline in degassing values from 120 Ma (Fig. 8), creating even lower simulated $CO_2$ levels during the Cenozoic.

## 7. Conclusions and challenges

By mapping out the areas of exposed land and reconstructing their spatial distribution for the past 520 Myrs, we have estimated the theoretical silicate weathering potential linked to land availability, here called 'total weatherability' (i.e. the equatorial regions and the northern and southern wet belts). Our new model predicts much larger variations in weatherability than previous models, notably for the Paleozoic, where we estimate the Phanerozoic maximum during the Ordovician and minimum during the Devonian.

This variability largely results from the amount of exposed land within the equatorial regions (±10°), and for most of the Paleozoic the continents were largely restricted to the southern hemisphere and there was no land in the northern continental wet belt.

The difference between exposed and total land at a given time provides an estimate of flooded land through time, which should closely track eustatic changes. The trends in our estimates of flooded land exhibit many similarities to the sea-level curve of Haq and Al-Qahtani (2005) and Haq and Schutter (2008) (Fig. 4c). Both show high values, albeit fluctuating, during mid-Ordovician to mid-Devonian times, lows during the time of Pangea (although somewhat offset in time), and a remarkably similar increase during Jurassic and Cretaceous times. This correspondence provides us with some additional confidence that our maps of exposed land provide reliable estimates.

To constrain plate tectonic degassing, we argue that normalized subduction flux is a reliable proxy. Subduction flux has been calculated from full-plate models back to the Early Devonian (410 Ma), and we observe two notable peaks during the early Carboniferous (~350 Ma) and the Early Cretaceous (~130 Ma), both periods of mild greenhouse conditions, whereas the LPIA and ECIA are characterized by a reduced subduction flux. As noted previously (e.g. Domeier et al. 2018), age distributions of arc-related zircons appear to grossly mimic subduction fluxes, and here we present a new approach to estimate degassing through time by rescaling the global zircon age distribution to the subduction flux. Importantly, this approach permits estimation of plate tectonic degassing in deep time when full-plate models become increasingly unreliable. Since the Late Devonian, there are some noticeable differences between the subduction flux and arc-activity, but mostly in the early Mesozoic, which could in part be an artefact of the plate model transition.

In general, our revised estimates for $f_A$ and $f_{AW}\_f_A$ (leaving all other parameters as in Royer et al. 2014) do not radically change modelled $CO_2$ levels but lead to somewhat higher levels in late Cambrian to Late Devonian times. Our results are (still) consistently lower than proxy estimates for the Mesozoic and especially Cenozoic times. However, if we normalize $f_{AW}\_f_A$ to the amount of exposed land within the tropics (±10°, $f_{AW10}\_f_A$), i.e. the regions with the highest potential $CO_2$ consumption by silicate weathering, and correct for arid equatorial areas between 270 and 110 Ma (as judged from biome maps), then there are rather dramatic changes in modelled $CO_2$. This results in a better model-proxy fit over the Mesozoic, but important discrepancies remain at 400 Ma and at the Permo-Triassic boundary. This better fit with refinements for aridity suggests that estimates of theoretical weatherability which assume static climatic belts (similar to those of the modern-day) could lead to poor estimation of land availability through time. Therefore, future enhancements in paleogeographic maps should focus on constraining climate gradients and linked land availability to weathering through time.

Leaving parameters as in Royer et al. (2014) and only implementing changes in $f_{SR}$ (based on normalized subduction flux to 380 Ma and thereafter normalized arc-activity) leads to rather lower $CO_2$ levels from the mid-Ordovician to the Early Devonian, slightly higher levels from the Devonian to the late Permian, and elevated highs in the Early Triassic (~250 Ma) and the Early Cretaceous (~130 Ma). The use of normalized arc-activity as a proxy for $f_{SR}$ improves slightly the model-proxy differences for Triassic to mid-Cretaceous times.

If we implement our changes in both $f_{SR}$ and $f_{AW}\_f_A$ in the GEOCARBSULFvolc model, improvements in the $CO_2$ model-proxy fit only occur in models constraining weatherability to ± 10° latitudes. These result in higher modelled $CO_2$ for the early to mid-Mesozoic and are in closer agreement with proxies. This is most evident in late Permian to mid-Cretaceous times, when (except for the elevated $CO_2$ peak at 250 Ma) modelled $CO_2$ levels for all our simulations are within the $CO_2$ proxies uncertainties envelope.

In conclusion, we consider our new estimates of $f_{SR}$ and $f_{AW}\_f_A$ to be important improvements to some of the key parameters in deep time $CO_2$ modelling. Nevertheless, $CO_2$ model-proxy mismatches remain, and clearly indicate a need for further revisions. Future research in enhancing long-term carbon cycle models should focus on constraining climate sensitivity through time, as well as better resolving the time-dependence of major $CO_2$ sinks and their dynamics, including carbon burial, the effects of plants on weathering (LIFE, GYM, FERT, and their time dependencies) and other poorly constrained parameters elaborated by Royer et al. (2014).

## Declaration of Competing Interest

The authors declare that they have no known competing financial interests or personal relationships that could have appeared to influence the work reported in this paper.

## Acknowledgments

We acknowledge financial support from the Research Council of Norway (RCN), through its Centres of Excellence funding scheme, project 223272 (CEED), and through RCN project 250111 to M.D. We also thank Tim Horscroft for this invited contribution. We thank Douwe van der Meer and two anonymous reviewers for their constructive comments that helped to improve the manuscript.

## Appendix A. Supplementary material

Supplementary data to this article can be found online at https://doi.org/10.1016/j.gr.2021.05.016.

## References

Abrajevitch, A., Van der Voo, R., 2010. Incompatible Ediacaran paleomagnetic directions suggest an equatorial geomagnetic dipole hypothesis. Earth Planet. Sci. Lett. 293 (1–2), 164–170.
Barrier, É., & Vrielynck, B. (2008). Paleotectonic maps of the Middle East: tectono-sedimentary-palinspatic maps from Late Norian to Pliocene, 14 maps, Comm. la Cart. Geol. du monde.
Barron, E.J., Hay, W.W., Thompson, S., 1989. The hydrologic cycle: a major variable during Earth history. Palaeogeo. Palaeoclim. Palaeoecol. 75 (3), 157–174.
Bergman, N.M., Lenton, T.M., Watson, A.J., 2004. COPSE: a new model of biogeochemical cycling over Phanerozoic time. Am. J. Sci. 304 (5), 397–437.
Berner, R.A., Lasaga, A.C., Garrels, R.M., 1983. The carbonate silicate geochemical cycle and its effect on atmospheric carbon dioxide over the past 100 million years. Am. J. Sci. 283, 641–683.
Berner, R.A., 2004. The Phanerozoic carbon cycle: CO2 and O2. Oxford University Press on Demand.
Berner, R.A., 2006. Inclusion of the weathering of volcanic rocks in the GEOCARBSULF model. Am. J. Sci. 306 (5), 295–302. https://doi.org/10.2475/05.2006.01.
Blakey, R. (2009). Molleweide plate tectonic maps. Available "on purchase" at https://deeptimemaps.com/.
Brune, S., Williams, S.E., Mueller, R.D., 2017. Potential links between continental rifting, CO2 degassing and climate change through time. Nature Geosci. 10 (12), 941–946.
Boucot, A.J., Xu, C., Scotese, C.R., Morley, R.J., 2013. Phanerozoic paleoclimate: an atlas of lithologic indicators of climate. SEPM (Society for Sedimentary Geology). ISBN:978-1-56576-282-4.
Cocks, L.R.M., Torsvik, T.H., 2020. Ordovician palaeogeography and climate change. Gond. Res. doi: 10.1016/j.gr.2020.09.008.
Caldeira, Ken, 1992. Enhanced Cenozoic chemical weathering and the subduction of pelagic carbonate. Nature 357 (6379), 578–581. https://doi.org/10.1038/357578a0.
Cogné, J.P., Humler, E., 2006. Trends and rhythms in global seafloor generation rate. Geochem. Geophys. Geosys. 7 (3).
Coltice, N., Seton, M., Rolf, T., Müller, R.D., Tackley, P.J., 2013. Convergence of tectonic reconstructions and mantle convection models for significant

fluctuations in seafloor spreading. Earth Planet. Sci. Lett. 383, 92–100.
Conrad, C.P., Lithgow-Bertelloni, C., 2007. Faster seafloor spreading and lithosphere production during the mid-Cenozoic. Geology 35, 29–32. https://doi.org/10.1130/G22759A.1.
Conrad, C.P., 2013. The solid Earth's influence on sea-level. GSA Bull. 125 (7–8), 1027–1052.
Crowley, T.J., 1991. Past CO2 changes and tropical sea surface temperatures. Paleoceanography 6 (3), 387–394.
Crowley, T.J., Baum, S.K., 1995. Reconciling Late Ordovician (440 Ma) glaciation with very high (14X) CO2 levels. J. Geophys. Res. 100, 1093–1101.
Dera, G., Brigaud, B., Monna, F., Laffont, R., Pucéat, E., Deconinck, J.F., Pellenard, P., Joachimski, M.M., Durlet, C., 2011. Climatic ups and downs in a disturbed Jurassic world. Geology 39 (3), 215–218.
Dercourt, J., Ricou, L.E., Vrielynck, B., (Eds.), 1993. Atlas Thethys Palaeoenvironmental Maps. Gauthier-Villars, Paris, 307p., 14 maps, 1 pl.
Dercourt, J., Gaetani, M., Vrielynck, B., Barrier E., Biju-Duval B., Brunet M.F., Cadet J. P., Crasquin, S., Sandulescu, M., (Eds.), 2000Atlas Peri-Thethys, Palaeogeographical maps. CCGM/CGMW, Paris: 24 maps and explanatory notes: I-XX; 1-269.
Domeier, M., Torsvik, T.H., 2014. Plate tectonics in the late Paleozoic. Geosci. Front. 5 (3), 303–350.
Domeier, M., 2016. A plate tectonic scenario for the Iapetus and Rheic oceans. Gond. Res. 36, 275–295. https://doi.org/10.1016/j.gr.2015.08.003.
Domeier, M., Magni, V., Hounslow, M.W., Torsvik, T.H., 2018. Episodic zircon age spectra mimic fluctuations in subduction. Sci. Rep. 8, 1747. https://doi.org/10.1038/s41598-018-35040-z.
Domeier, M., 2018. Early Paleozoic tectonics of Asia: Towards a full-plate model. Geosci. Front. 9, 789–862. https://doi.org/10.1016/j.gsf.2017.11.012.
Donnadieu, Y., Pierrehumbert, R., Jacob, R., Fluteau, F., 2006. Modelling the primary control of paleogeography on Cretaceous climate. Earth Planet. Sci. Lett. 248 (1–2), 426–437.
Ebelmen, J.J., 1845. Sur les produits de la decomposition des especes minirales de la famille des silicates. Annales des Mines 7, 3–66.
Engebretson, D.C., 1992. 180 million years of subduction. GSA today 2, 100.
Fielding, C.R., Frank, T.D., Isbell, J.L., 2008. The late Paleozoic ice age — A review of current understanding and synthesis of global climate patterns. In: Fielding, C. R., Frank, T.D., Isbell, J.L. (Eds.), Resolving the Late Paleozoic Ice Age in Time and Space. GSA Special Paper, 441, 343-354, doi: 10.1130/2008.2441(24).
Foster, G.L., Royer, D.L., Lunt, D.J., 2017. Future climate forcing potentially without precedent in the last 420 million years. Nature Commun. 8, 14845.
Francois, L.M., Walker, J.C., 1992. Modelling the Phanerozoic carbon cycle and climate: constraints from the 87Sr/86Sr isotopic ratio of seawater. Am. J. Sci 292 (2), 81–135.
Gibbs, M.T., Bluth, G.J., Fawcett, P.J., Kump, L.R., 1999. Global chemical erosion over the last 250 my; variations due to changes in paleogeography, paleoclimate, and paleogeology. Am. J. Sci. 299 (7–9), 611–651.
Gibbs, M.T., Bice, K.L., Barron, E.J., Kump, L.R., 2000. Glaciation in the early Paleozoic 'greenhouse': the roles of paleogeography and atmospheric CO2. In: Huber, B.T., MacLeod, K.G., Wing, S.L., Eds., Warm Climates in Earth History. Cambridge, Cambridge University Press, pp. 386-422.
Goddéris, Y., François, L.M., 1995. The Cenozoic evolution of the strontium and carbon cycles: relative importance of continental erosion and mantle exchanges. Chem. Geol. 126 (2), 169–190.
Goddéris, Y., Joachimski, M.M., 2004. Global change in the Late Devonian: modelling the Frasnian-Famennian short-term carbon isotope excursions. Palaeogeo. Palaeoclim. Palaeoecol. 202 (3–4), 309–329.
Goddéris, Y., Donnadieu, Y., Lefebvre, V., Le Hir, G., Nardin, E., 2012. Tectonic control of continental weathering, atmospheric $CO_2$, and climate over Phanerozoic times. C. R. Geo. 344 (11–12), 652–662. https://doi.org/10.1016/j.crte.2012.08.009.
Goddéris, Y., Donnadieu, Y., Le Hir, G., Lefebvre, V., Nardin, E., 2014. The role of paleogeography in the Phanerozoic history of atmospheric $CO_2$and climate. Earth Sci. Rev. 128, 122–138. https://doi.org/10.1016/j.earscirev.2013.11.004.
Goddéris, Y., Donnadieu, Y., 2017. A sink- or a source-driven carbon cycle at the geological timescale? Relative importance of paleogeography versus solid Earth degassing rate in the Phanerozoic climatic evolution. Geol. Mag. 156 (2), 355–365. https://doi.org/10.1017/S0016756817001054.
Goddéris, Y., Donnadieu, Y., Carretier, S., Aretz, M., Dera, G., Macouin, M., Regard, V., 2017. Onset and ending of the late Palaeozoic ice age triggered by tectonically paced rock weathering. Nature Geosci. 10 (5), 382–386.
Goldberg, S.L., Present, T.M., Finnegan, S., Bergmann, K.D., 2021. A high-resolution record of early Paleozoic climate. PNAS 118, (6) e2013083118.
Golonka, J., Krobicki, M., Pajak, J., Van Giang, N., Zuchiwwicz, W., 2006. Global Plate Tectonics and Paleogeography of Southeast Asia, Faculty of Geology. Geophysics and Environmental Protection. AGH University of Science and Technology, Arkadia, Krakow, Poland.
Gyllenhaal, E.D., Engberts, C.J., Markwick, P.J., Smith, L.H., Patzkowsky, M.E., 1991. The Fujita-Ziegler model: a new semi-quantitative technique for estimating paleoclimate from paleogeographic maps. Palaeogeo., Palaeoclim., Palaeoecol. 86 (1–2), 41–66.
Hansen, James, Sato, Makiko, Kharecha, Pushker, Beerling, Davis, Berner, Robert, Masson-Delmotte, Valerie, Pagani, Mark, Raymo, Maureen, Royer, Dana L., Zachos, James C., 2008. Target Atmospheric CO2: Where Should Humanity Aim? Open Atmospheric Science Journal 2, 217–231. https://doi.org/10.2174/1874282300802010217.
Haq, B.U., Al-Qahtani, A.M., 2005. Phanerozoic cycles of sea-level change on the Arabian Platform. GeoArabia 10 (2), 127–160.
Haq, B.U., Schutter, S.R., 2008. A chronology of Paleozoic sea-level changes. Science 322 (5898), 64–68.
Hartman, G., Richards, M., 2014. Mapping and defining sources of variability in bioavailable strontium isotope ratios in the Eastern Mediterranean. Geochim. Cosmochim. Acta 126, 250–264.
Hay, W.W., Barron, E.J., Thompson, S.L., 1990. Global atmospheric circulation experiments on an Earth with polar and tropical continents. J. Geo. Soc. 147 (5), 749–757.
Heine, C., Yeo, L.G., Müller, R.D., 2015. Evaluating global paleoshoreline models for the Cretaceous and Cenozoic. Aust. J. Earth Sci. 62 (3), 275–287.
Herrmann, A.D., Patzkowsky, M.E., Pollard, D., 2003. Obliquity forcing with 8–12 times preindustrial levels of atmospheric $pCO_2$ during the Late Ordovician glaciation. Geology 31, 485–488.
Hilley, G.E., Porder, S., 2008. A framework for predicting global silicate weathering and CO2 drawdown rates over geologic time-scales. Proc. Natl. Acad. Sci. USA 105 (44), 16855–16859.
Horton, D.E., Poulsen, C.J., Pollard, D., 2010. Influence of high-latitude vegetation feedbacks on late Palaeozoic glacial cycles. Nat. Geosci. 3 (8), 572–577.
Hounslow, M.W., Domeier, M., Biggin, A., 2018. Subduction flux modulates the geomagnetic polarity reversal rate. Tectonophysics 742, 34–49.
Karlsen, K.S., Domeier, M., Gaina, C., Conrad, C.P., 2020. A tracer-based algorithm for automatic generation of seafloor age grids from plate tectonic reconstructions. Comput.Geosci. 104508.
Kump, L.R., Arthur, M.A., Patzkowsky, M.E., Gibbs, M.T., Pinkus, D.S., Sheehan, P.M., 1999. A weathering hypothesis for glaciation at high atmospheric pCO2 during the Late Ordovician. Palaeogeo. Palaeoclim. Palaeoecol. 152 (1–2), 173–187.
Lagabrielle, Y., Goddéris, Y., Donnadieu, Y., Malavieille, J., Suarez, M., 2009. The tectonic history of Drake Passage and its possible impacts on global climate. Earth Planet. Sci. Lett. 279 (3–4), 197–211.
Larson, R.L., 1991. Geological consequences of superplumes. Geology 19 (10), 963–966.
Lee, C.T.A., Lackey, J.S., 2015. Global continental arc flare-ups and their relation to long-term greenhouse conditions. Elements 11 (2), 125–130.
Lee, C-T.A., Jiang, H., Dasgupta, R., Torres, M., 2020. A framework for understanding whole-earth carbon cycling. In: Orcutt, B., Daniel, I., Dasgupta, R. (Eds.), DEEP CARBON: Past to Present. Cambridge University Press, pp. 313–357. doi:10.1017/9781108677950.
Lenton, T.M., Daines, S.J., Mills, B.J., 2018. COPSE reloaded an improved model of biogeochemical cycling over Phanerozoic time. Earth Sci. Rev. 178, 1–28.
Lowry, D.P., Poulsen, C.J., Horton, D.E., Torsvik, T.H., Pollard, D., 2014. Thresholds for Paleozoic ice sheet initiation. Geology 42, 627–630.
Lyell, C. (1830). Principles of geology, being an attempt to explain the former changes of the Earths surface, by reference to causes now in operation. London, John Murray, Volume 1.
Marshall, H.G., Walker, J.C., Kuhn, W.R., 1988. Long-term climate change and the geochemical cycle of carbon. J. Geophys. Res.: Atmospheres 93 (D1), 791–801.
Matthews, K., Maloney, K.T., Zahirovic, S., Williams, S.E., Seton, M., Müller, R.D., 2016. Global plate boundary evolution and kinematics since the late Paleozoic. Glob. Planet. Chang. 146, 226–250.
McKenzie, N.R., Horton, B.K., Loomis, S.E., Stockli, D.F., Planavsky, N.J., Lee, C.-T.A., 2016. Continental arc volcanism as the principal driver of icehouse-greenhouse variability. Science 352 (6284), 444–447. https://doi.org/10.1126/science.aad5787.
Merdith, A.S., Williams, S.E., Brune, S., Collins, A.S., Müller, R.D., 2019. Rift and plate boundary evolution across two supercontinent cycles. Glob. Planet. Chang. 173, 1–14.
Merdith, A.S., Williams, S.E., Collins, A.S., Tetley, M.G., Mulder, J.A., Blades, M.L., Young, A., Armistead, S.E., Cannon, J., Zahirovic, S., Müller, R.D., 2021. Extending full-plate tectonic models into deep time: Linking the Neoproterozoic and the Phanerozoic. Earth Sci. Rev. 214. https://doi.org/10.1016/j.earscirev.2020.103477.
Michel, L.A., Tabor, N.J., Montañez, I.P., Schmitz, M.D., Davydov, V.I., 2015. Chronostratigraphy and paleoclimatology of the Lodève Basin, France: evidence for a pan-tropical aridification event across the Carboniferous-Permian boundary. Palaeogeo. Palaeoclim. Palaeoecol. 430, 118–131.
Mills, B., Daines, S.J., Lenton, T.M., 2014. Changing tectonic controls on the long-term carbon cycle from Mesozoic to present. Geochem. Geophys. Geosys. 15 (12), 4866–4884.
Mills, B.J., Scotese, C.R., Walding, N.G., Shields, G.A., Lenton, T.M., 2017. Elevated CO 2 degassing rates prevented the return of Snowball Earth during the Phanerozoic. Nat. comm. 8 (1), 1–7.
Mills, B.J.W., Krause, A.J., Scotese, C.R., Hill, D.J., Shields, G.A., Lenton, T.M., 2019. Modelling the long-term carbon cycle, atmospheric $CO_2$, and Earth surface temperature from late Neoproterozoic to present day. Gond. Res. 67, 172–186.
Montañez, I.P., Poulsen, C.J., 2013. The Late Paleozoic Ice Age: An Evolving Paradigm. Annu. Rev. Earth Planet. Sc. 41, 629–656. https://doi.org/10.1146/annurev.earth.031208.100118.
Moore, T.L., Scotese, C.R., 2010. The Paleoclimate Atlas (ArcGIS), GSA, 2010 Annual Meeting. Abstracts with Programs 42, 598.
Mujal, E., Fortuny, J., Marmi, J., Dinarès-Turell, J., Bolet, A., Oms, O., 2018. Aridification across the Carboniferous-Permian transition in central equatorial Pangea: the Catalan Pyrenean succession (NE Iberian Peninsula). Sediment. Geol. 363, 48–68.
Ollier, C., Pain, C., 1996. Regolith, Soils and Landforms. John Wiley & Sons.
Oki, T., & Kanae, S. (2006). Global hydrological cycles and world water resources. Science, 313(5790), 1068–1072.

Otto-Bliesner, B.L., 1995. Continental drift, runoff, and weathering feedbacks: implications from climate model experiments. J. Geophys. Res. 100 (6), 11537–11548.
Pagani, Mark, Liu, Zhonghui, laRiviere, Jonathan, Ravelo, Ana Christina, 2010. High Earth-system climate sensitivity determined from Pliocene carbon dioxide concentrations. Nature Geoscience 3, 27–30. https://doi.org/10.1038/ngeo724.
Park, J., Royer, D.L., 2011. Geologic constraints on the glacial amplification of Phanerozoic climate sensitivity. Am. J. Sci. 311 (1), 1–26.
Poblete, F., Dupont-Nivet, G., Licht, A., Van Hinsbergen, D.J., Roperch, P., Mihalynuk, M.G., et al., 2021. Towards interactive global paleogeographic maps, new reconstructions at 60, 40 and 20 Ma. Earth Sci. Rev. 103508.
Pohl, A., Donnadieu, Y., Le Hir, G., Buoncristiani, J.F., Vennin, E., 2014. Effect of the Ordovician paleogeography on the (in) stability of the climate. Clim. Past 10 (6), 2053–2066.
Puetz, S.J., Ganade, C.E., Zimmermann, U., Borchardt, G., 2018. Statistical Analyses of Global U-Pb Database 2017. Geosci. Front. 9, 121–145.
Rohling, E et al.PALAEOSENS Project Members, 2012. Making sense of palaeoclimate sensitivity. Nature 491, 683–691. https://doi.org/10.1038/nature11574.
Rowley, D.B., 2002. Rate of plate creation and destruction: 180 Ma to present. GSA Bull. 114 (8), 927–933.
Royer, D.L., 2006. CO2-forced climate thresholds during the Phanerozoic. Geochim. Cosmochim. Acta 70 (23), 5665–5675. https://doi.org/10.1016/j.gca.2005.11.031.
Royer, D.L., Donnadieu, Y., Park, J., Kowalczyk, J., Goddéris, Y., 2014. Error analysis of CO2 and O2 estimates from the long-term geochemical model GEOCARBSULF. Am. J. Sci. 314 (9), 1259–1283.
Royer, D.L., 2016. Climate sensitivity in the geologic past. Annu. Rev. Earth Planet Sci., 44
Sahney, S., Benton, M.J., Falcon-Lang, H.J., 2010. Rainforest collapse triggered Carboniferous tetrapod diversification in Euramerica. Geology 38 (12), 1079–1082.
Schellart, W., Stegman, D., Freeman, J., 2008. Global trench migration velocities and slab migration induced upper mantle volume fluxes: constraints to find an Earth reference frame based on minimizing viscous dissipation. Earth Sci. Rev. 88, 118–144.
Scotese, C.R., 2014a. The PALEOMAP Project PaleoAtlas for ArcGIS, version 2, Volume 1, Cenozoic Plate Tectonic, Paleogeographic, and Paleoclimatic Reconstructions, Maps 1-15. PALEOMAP Project, Evanston.
Scotese, C.R., 2014b. Atlas of Paleogene Paleogeographic Maps (Mollweide Projection), Maps 8–15, Volume 1, The Cenozoic, PALEOMAP Atlas for ArcGIS. Evanston, IL, USA: PALEOMAP Project.
Scotese, C.R., Moore, T.L., 2014. Atlas of Phanerozoic Ocean Currents and Salinity (Mollweide Projection),Volumes 1-6, PALEOMAP Project PaleoAtlas for ArcGIS, PALEOMAP Project, Evanston, IL.
Scotese, C.R., 2016. PALEOMAP PaleoAtlas for GPlates and the PaleoData plotter program. In: GSA Abstracts with Programs, vol. 48, No. 5.
Scotese, C.R., Song, H., Mills, B.J.W., van der Meer, D.G., 2021. Phanerozoic paleotemperatures: The Earth's changing climate during the last 540 million years. Earth Sci. Rev.
Seton, M., Gaina, C., Müller, R.D., Heine, C., 2009. Mid-Cretaceous seafloor spreading pulse: fact or fiction?. Geology 37 (8), 687–690.
Seton, M., Müller, R.D., Zahirovic, S., Gaina, C., Torsvik, T.H., Shephard, G., Talsma, A., Gurnis, M., Turner, M., Chandler, M., 2012. Global continental and ocean basin reconstructions since 200 Ma. Earth Sci. Rev. 113, 212–270.
Song, H., Wignall, P.B., Song, H., Dai, X., Chu, D., 2019. Seawater temperature and dissolved oxygen over the past 500 million years. J. Earth Sci. 30 (2), 236–243.
Soreghan, G.S., Soreghan, M.J., Heavens, N.G., 2019. Explosive volcanism as a key driver of the late Paleozoic ice age. Geology 47, 600–604. https://doi.org/10.1130/G46349.1.
Torsvik, T.H., Steinberger, B., Gurnis, M., Gaina, C., 2010. Plate tectonics and net lithosphere rotation over the past 150 My. Earth Planet. Sci. Lett. 291, 106–112.
Torsvik, T.H., van der Voo, R., Doubrovine, P.V., Burke, K., Steinberger, B., Ashwal, L. D., Trønnes, R.G., Webb, S.J., Bull, A.L., 2014. Deep mantle structure as a reference frame for movements in and on the Earth. Proc. Natl. Acad. Sci. USA 111, 8735–8740. https://doi.org/10.1073/pnas.1318135111.
Torsvik, T.H., Cocks, L.R.M., 2017. Earth History and Palaeogeography. Cambridge University Press. 317 pp..
Torsvik, T.H., Steinberger, B., Shephard, G.E., Doubrovine, P.V., Domeier, M., Gaina, C., Conrad, C., Sager, W.W., 2019. Pacific-Panthalassic reconstructions: Overview, errata and the way forward. Geochem. Geophys. Geosys. 20. https://doi.org/10.1029/2019GC008402.
Torsvik, T.H., Svensen, H.H., Steinberger, B., Royer, D.L., Jerram, D.A., Jones, M.T., Domeier, M., 2020. Connecting the Deep Earth and the Atmosphere. AGU book chapter.
Vandenbroucke, T.R., Armstrong, H.A., Williams, M., Paris, F., Zalasiewicz, J.A., Sabbe, K., et al., 2010. Polar front shift and atmospheric CO2 during the glacial maximum of the Early Paleozoic Icehouse. Proc. Natl. Acad. Sci. 107 (34), 14983–14986.
Van der Meer, D.G., Torsvik, T.H., Spakman, W., Van Hinsbergen, D.J.J., Amaru, M.L., 2012. Intra-Panthalassa Ocean subduction zones revealed by fossil arcs and mantle structure. Nat. Geo. 5 (3), 215–219.
Van der Meer, D.G, Zeebe, R., van Hinsbergen, D.J.J., Sluijs, A., Spakman, W., Torsvik, T.H., 2014. Plate tectonic controls on atmospheric CO2 levels since the Triassic. Proc. Natl. Acad. Sci. doi:10.1073/ pnas.1315657111.
Voice, P.J., Kowalewski, M., Eriksson, K.A., 2011. Quantifying the timing and rate of crustal evolution: global compilation of radiometrically dated detrital zircon grains. J. Geol. 119, 109–126.
Walker, J.C.G., Hays, P.B., Kasting, J.F., 1981. A negative feedback mechanism for the long-term stabilization of Earth's surface temperature. J. Geophys. Res. 86, 9776–9782.
Wegener, A., 1912. Die Entstehung der Kontinente. Dr. A. Petermanns Mitteilungen aus Justus Perthes geographischer Anstalt, 58, 185–195, 253–256, 305–309.
West, A.J., Galy, A., Bickle, M., 2005. Tectonic and climatic controls on silicate weathering. Earth Planet. Sci. Lett. 235 (1–2), 211–228.
White, A.F., Blum, A.E., 1995. Effects of climate on chemical_ weathering in watersheds. Geochim. Cosmochim. Acta 59 (9), 1729–1747.
Witkowski, C.R., Weijers, J.W., Blais, B., Schouten, S., Damsté, J.S.S., 2018. Molecular fossils from phytoplankton reveal secular PCO2 trend over the Phanerozoic. Sci. Adv. 4(11), eaat4556.
Witkowski, C.R., Agostini, S., Harvey, B.P., Van Der Meer, M.T., Sinninghe Damsté, J. S., Schouten, S., 2019. Validation of carbon isotope fractionation in algal lipids as a pCO 2 proxy using a natural CO 2 seep (Shikine Island, Japan). Biogeosciences 16 (22), 4451–4461.
Wong, K., Mason, E., Brune, S., East, M., Edmonds, M., Zahirovic, S., 2019. Deep carbon cycling over the past 200 million years: a review of fluxes in different tectonic settings. Front. Earth Sci. 7, 263. https://doi.org/10.3389/feart.2019.00263.
Worsley, T.R., Kidder, D.L., 1991. First-order coupling of paleogeography and CO sub 2, with global surface temperature and its latitudinal contrast. Geology 19(12). doi: 10.1130/0091-7613(1991)019<1161: FOCOPA>2.3.CO; 2.
Wotte, T., Skovsted, C.B., Whitehouse, M.J., et al., 2019. Isotopic evidence for temperate oceans during the Cambrian Explosion. Sci. Rep. 9, 6330.
Young, A., Flament, N., Maloney, K., Williams, S., Matthews, K., Zahirovic, S., Müller, R.D., 2019. Global kinematics of tectonic plates and subduction zones since the late Paleozoic Era. Geosci. Front. 10, 989–1013. https://doi.org/10.1016/j.gsf.2018.05.011.
Zhang, X., Prange, M., Steph, S., Butzin, M., Krebs, U., Lunt, D.J., Schulz, M., 2012. Changes in equatorial Pacific thermocline depth in response to Panamanian seaway closure: Insights from a multi-model study. Earth Planet. Sci. Lett. 317, 76–84.
Ziegler, P.A., 1990. Geological atlas of western and central Europe. Shell Internationale Petroleum Maatschappij BV, 239 pp.

**Chloé M. Marcilly** PhD research fellow at the Centre for Earth Evolution and Dynamics (CEED), at the Department of Geosciences, University of Oslo since 2019. She completed a MSc in sedimentology/geochemistry from the University of Oslo in 2016. She is working within the field of paleoclimate reconstructions and long-term carbon cycle modelling. Her main research interest is the effect of changing paleogeography and carbon degassing on climate over geological timescales.

**Trond H. Torsvik** Professor of Geodynamics and Director of the Centre for Earth Evolution and Dynamics (CEED), University of Oslo (Norway). He is also a Professor at Wits University (Johannesburg, South Africa) and with particular interests in paleomagnetism, paleogeography, Earth history and long-term climate evolution.

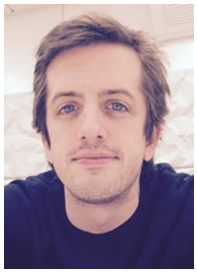

**Mathew Domeier** Researcher at the Centre for Earth Evolution and Dynamics (CEED) at the University of Oslo (Norway) since 2013, with research interests in tectonics, paleogeography and paleomagnetism.

**Dana L. Royer** Professor of Earth and Environmental Sciences at Wesleyan University (USA). He is interested in $CO_2$ proxies, long-term carbon cycle models, and understanding patterns of $CO_2$ and climate sensitivity over the Phanerozoic.